A&A, 707, A65 (2026)
https://doi.org/10.1051/0004-6361/202556733

Astronomy & Astrophysics

Morphologies arising from the gas flow in the innermost kiloparsec of barred galaxy models

S. Pastras[1,2,⋆], P. A. Patsis[3,2,⋆], and E. Athanassoula[4,⋆]

[1] Max-Planck-Institut für Extraterrestrische Physik (MPE), Gießenbachstr. 1, D-85748 Garching, Germany
[2] Max-Planck-Institut für Astrophysik (MPA), Karl-Schwarzschild-Str. 1, D-85748 Garching, Germany
[3] Research Center for Astronomy and Applied Mathematics, Academy of Athens, Soranou Efessiou 4, 11527 Athens, Greece
[4] Aix Marseille Université, CNRS, LAM (Laboratoire d' Astrophysique de Marseille), UMR 7326, 13388 Marseille 13, France

Received 4 August 2025 / Accepted 23 November 2025

ABSTRACT

Context. We study a series of response models to investigate the formation of specific morphological features in the central 1 kpc region of the gas component in barred spiral galaxies.
Aims. We aim to understand how structures, such as nuclear rings and spirals, form by varying the parameters of a general gravitational potential and gas properties. Our goal is to determine how much the shape of these structures is driven by the orbital dynamics of the models compared to the influence of the hydrodynamics of the gas. In particular, we examine the effects of the bar strength, bar shape, pattern speed, and central density, as well as their mutual interdependence.
Methods. We modeled the gas flow using hydrodynamical simulations run with the Eulerian RAMSES code. The underlying gravitational potential was a two-dimensional Ferrers bar and the gas was considered to be isothermal. Alongside analyzing the gas response to the imposed gravitational potentials, we carried out orbital studies for all models. This involved assessing the shapes and stability of periodic orbits and analyzing the distribution of regular versus chaotic regions within the systems.
Results. The parameters of the gravitational potential alone are insufficient to accurately predict the gas dynamics in a system. The morphology of the gaseous response varies substantially with changes in sound speed, emphasizing the fundamental role of hydrodynamic processes in determining the structure of the gas within the central region. We identify the factors that affect the morphology of nuclear rings and trailing and leading nuclear spirals. The best alignment between our models and structures observed in local barred galaxies is achieved by assuming a sound speed of $c_s = 20\,\mathrm{km\,s^{-1}}$.

Key words. chaos – ISM: kinematics and dynamics – galaxies: kinematics and dynamics

1. Introduction

The innermost kiloparsec of a galactic bar is its central region, which in some cases includes an area encircled by a nuclear ring (see for example Comerón et al. 2010) along with the nuclear ring itself. Observations provide sufficient information about the topology and the general morphology of nuclear rings, allowing even for their classification into subclasses (Buta & Combes 1996; Comerón et al. 2010).

However, the area within these rings is less explored. The primary challenges for observing structures within the innermost kiloparsec are resolution and projection effects. There are significantly fewer studies that attempt to identify common morphological features in the central regions of galaxies and connect them to the dynamics of the parent bar.

Notably Martini et al. (2003a,b) used *HST* images of an extensive galaxy sample to map the distribution of the cold interstellar medium in the central parts of disk galaxies using dust as a tracer. Among the observed morphologies, they identified nuclear dust spirals, which could be categorized as grand design, tightly wound, loosely wound, or chaotic (flocculent). In certain instances, they also detected chaotic circumnuclear dust within the innermost kiloparsec, or, in some cases, the absence of any circumnuclear dust structure. Their findings indicated a connection between grand design nuclear spirals and large-scale bars. Contrarily, they found that tightly wound nuclear spiral arms are more commonly observed in unbarred galaxies rather than in barred ones.

Furthermore, Martini et al. (2003a,b) revealed that the majority of barred galaxies do not exhibit rings inside the bar, implying that nuclear spirals are often not situated within a nuclear ring. In such instances, they are linked directly to the relatively straight dust lanes that are associated with the large-scale bar. In such cases, the dust lanes essentially form continuous structures spanning from scales of several kiloparsecs down to within tens of parsecs from the galactic center. Such an example is that of NGC 1530 (see for example Buta 2013, – figure 1-25), in which a curve is observed in the primary dust lanes of the bar near the center, without the clear presence of a nuclear ring.

Nevertheless, the regions inside the rings are not always featureless. An example of grand design spiral arms inside a nuclear ring is observed in the recently released *JWST* image of NGC 1433. Patsis et al. (2021) identified a nuclear trailing spiral embedded within the peanut-shaped bulge of NGC 352. Another example, this time of a multiarmed spiral, is identified inside the nuclear ring of NGC 1512 as observed by the Hubble space telescope. There are also cases in which the nuclear spiral has three arms, as in the case of NGC 1097, where a three-armed spiral can

⋆ Corresponding authors: spastras@mpe.mpg.de; patsis@academyofathens.gr; lia@lam.fr

be identified inside a nuclear ring (Prieto et al. 2005; Fathi et al. 2006; Davies et al. 2009) (however, see also Kolcu et al. 2023).

Regarding the nuclear rings themselves, in numerous cases they exhibit a pseudo-ring nature, appearing as an extension of the primary dust lane shocks. The surface density is not uniform along a ring and the denser segments are located in the quadrants that extend inward from the primary shocks. Because of this, they can be referred to as pseudo-rings. Typical examples can be observed, for instance, in the SDSS image of NGC 5383, in the ring of NGC 4736 (van der Laan et al. 2015), or in the *HST* image of NGC 1512. This class of pseudo-rings can be viewed as displaying a morphology that lies between those with well-defined nuclear rings and those where the main dust lane shocks curve inward, extending into the region within 1 kpc.

Another morphological feature associated with the central regions of barred galaxies, and predicted by the gaseous density wave theory in its linear approximation (Goldreich & Tremaine 1978, 1979), is the formation of leading spirals. They are expected to appear at the inner inner Lindblad resonance (iILR) region propagating outward (see for example Maciejewski 2004a), provided that this resonance exists. Nevertheless, there are not many known examples of leading spirals in the innermost kiloparsec regions of galactic disks. We mention the K′ image of NGC 6902 (Grosbøl 2003), which however is a Sa(r) type galaxy. Another compelling case is that of M100 (NGC 4321), with observations and models presented in Knapen et al. (1995a,b). Additionally, Díaz et al. (2003) reported the presence of a well-defined two-armed leading spiral inside a nuclear ring observed in Paα emission at the core of NGC 1241. In this case, farther inward, a tiny bar could also be identified.

Central leading spirals have been simulated in analytic models and models of the gas response to bar potentials, under various assumptions. These spirals are anticipated to manifest in the gaseous orbits of weak bar potentials, irrespective of whether the effects of self-gravity are considered (Wada 1994; Wada & Koda 2001; Maciejewski 2004a). They have been reproduced in hydrodynamical simulations by Ann & Thakur (2005) using smoothed particle hydrodynamics (SPH), by Kim et al. (2012b,a) using the grid-based code `CMHOG` (Piner et al. 1995), by Sormani et al. (2015b) by means of a second-order flux-splitting scheme (van Albada et al. 1982; Athanassoula 1992b) and by Li et al. (2015) using the grid-based magnetohydrodynamics code `Athena` (Stone et al. 2008), which utilizes a higher-order Godunov scheme (Stone & Gardiner 2009).

The presence of leading nuclear spirals in models with ILRs is claimed to be linked to the variation in the precession rate of elliptical periodic orbits. They emerge when the shape of the $\Omega - \kappa/2$ curve in its innermost part is decreasing toward the center. Here, Ω represents the angular frequency and κ denotes the epicyclic frequency. On the contrary, if this curve increases toward the center, for instance, due to the presence of a central massive black hole (MBH), the gas forms a trailing spiral. This scenario is aptly elucidated in Buta & Combes (1996, – figure 79) and Combes (2022, – figure 2).

It is puzzling that nuclear leading spirals are rarely observed in images of barred spiral galaxies. This is surprising considering that in the typical cases of standard barred galaxy potentials, the $\Omega - \kappa/2$ curves tend to decrease toward the center, allowing the coexistence of an iILR and an outer ILR (oILR) (see e.g., Contopoulos 1980, – figure 1) for a wide range of realistic bar pattern speeds. Nevertheless, it is indeed true that, despite being predicted in some cases, nuclear leading spirals do not form in all hydrodynamic simulations. This discrepancy may stem either from the extent of the trailing spirals produced at the oILR, numerical issues related to the simulation itself, such as the resolution of the numerical scheme employed (Maciejewski 2004b), or because they are simply a transient feature (Ann & Thakur 2005).

In this study, we investigate the circumstances that lead to the appearance of all these morphological features within the central regions of the gaseous components of barred galaxies in models that do not explicitly include a black hole, represented by a point mass. Several numerical studies of bar-induced flows in isothermal gas disks have examined how the resulting structures depend on the adopted sound speed, using a variety of different imposed potentials (e.g., Englmaier & Gerhard 1997; Patsis & Athanassoula 2000; Maciejewski et al. 2002; Slyz et al. 2003; Kim et al. 2012b; Sormani et al. 2015a). Other works focus on the effects of various potential parameters, but do not additionally explore the dependence of the resulting morphologies on the sound speed of the gas (e.g, Regan & Teuben 2003; Kim et al. 2012a). Unlike previous works, our study systematically investigates the effects of multiple parameters on the formation of nuclear spirals, all within a single, general Ferrers bar potential, and in each case for an array of different gas sound speeds. By varying only one parameter at a time while keeping the others fixed, we are able to isolate its individual influence on the gas response in the innermost kiloparsec.

Our objective is to understand how variations in the underlying gravitational potential and gas properties affect the formation of nuclear rings and nuclear spirals. We aim to determine the extent to which the resulting shapes of such structures are influenced by the orbital characteristics of our models versus the hydrodynamics of the gas. Particular emphasis is put on less explored factors, such as the influence of the bar shape, bar strength, pattern speed, and central density of the imposed potential. We also focus on how the sound speed governs the emergence of leading spirals within nuclear rings.

We use a grid-based hydrodynamical code with a spatial resolution high enough to resolve structures within the central kiloparsec, allowing us to capture the nuclear features in detail. This represents a complement to the classic study by Athanassoula (1992b), which successfully resolved shocks in the main bar region but did not examine the gas response in the central parts of the models.

In Section 2, we provide details regarding the general potential used, the specific cases we analyzed, the hydrocode employed, and the way we approach the stellar dynamics of the examined cases. Subsequently, in Section 3, we present the orbital content of the models and the response of the gas in the five cases we have considered. To assess the influence of the bar component in our models, we compare the primary results from Section 3 with models of extremely weak bars in Section 4. Section 5 contains our discussion and summarizes our conclusions.

2. The models we studied

2.1. The gravitational potential

In our study, we adopted the general gravitational potential used by Athanassoula (1992a), which encompasses three components representing a bulge, a disk, and a bar. The bulge has a volume density of

$$\rho(r) = \rho_b \left(1 + \frac{r^2}{{r_b}^2}\right)^{-3/2}, \tag{1}$$

with ρ_b and r_b being, respectively, the bulge central density and scale length.

Table 1. Dynamical parameters of the five main models.

Model	a/b	r_L	$Q_m/10^4$	$\rho_c/10^4$	Ω_B
R001	2.5	6.0	4.5	2.4	35.300
R010	1.5	6.0	4.5	2.4	35.437
R153	2.5	3.0	4.5	2.4	77.726
R192	2.5	6.0	1.5	2.4	33.662
R901	2.5	6.0	4.5	20.0	35.615

The surface density of the disk is given by

$$\sigma(r) = \frac{v_0^2}{2\pi G r_0}\left(1 + \frac{r^2}{r_0{}^2}\right)^{-3/2}, \tag{2}$$

with v_0 and r_0 being scaling constants, i.e., it is a Kuzmin-Toomre disk (Kuzmin 1956; Toomre 1963).

The bar is a standard Ferrers ellipsoid (Ferrers 1877) with volume density

$$\rho_B(x,y,z) = \begin{cases} \rho_0(1-g^2) & \text{for } g < 1 \\ 0 & \text{elsewhere,} \end{cases} \tag{3}$$

with

$$g^2 = \frac{y^2}{a^2} + \frac{x^2+z^2}{b^2}, \text{and } a > b, \text{with } a = 5\,\text{kpc}.$$

The quadrupole moment, Q_m, of the bar along its major axis, q_y, is given by

$$q_y = 2M_B(a^2 - b^2)/7 = 2Q_m, \tag{4}$$

where M_B is the mass of the bar.

The units used for the model parameters are, $10^6\,M_\odot$ for the mass, 1 kpc for the length, and $1\,\text{km}\,\text{s}^{-1}$ for the velocity. The resulting angular frequency, Ω, unit is $1\,\text{km}\,\text{s}^{-1}\,\text{kpc}^{-1}$. For further details the reader may refer to Athanassoula (1992a).

This model enables us to explore the dynamics of bars in their central regions for different parameter sets. Its straightforward nature facilitates the correlation of particular dynamical behaviors with variations in specific parameters, thereby assessing the significance of these parameters in relation to the emergence of specific morphological features. Moreover, this potential has been thoroughly studied in the literature, making direct comparisons with previous research possible.

Specifically, we examined five models characterized by typical bar parameters. Four of these are listed in Athanassoula (1992a, – table 1). We chose to keep the same reference numbers for these four cases. The fifth model (R901) was included to explore a different case with a noticeably unique shape in its rotation curve compared to the others.

The parameters characterizing these models are summarized in Table 1. In the table, we give, from left to right, the name of the model, the bar axial ratio a/b, the radius of the L_1 and L_2 Lagrangian points, a measure of the quadrupole moment of the bar along its major axis, Q_m (see Eq. (4)), the sum of the bar and bulge central density, $\rho_c = \rho_0 + \rho_b$, and the pattern speed of the bar, Ω_B.

Moreover, we examined two additional cases, with parameters resembling those of models R001 and R901, except that these models featured an extremely weak bar, effectively making them nearly axisymmetric (as we explain in Section 4). This was carried out to assess the significance of the gravitational forces relative to the hydrodynamical characteristics of the gas in determining the fundamental conclusions of our study.

2.2. Modeling the gas flow

To model the gas flow, we conducted a series of hydrodynamic simulations using the Eulerian `RAMSES` code (Teyssier 2002), which has been effectively applied in similar gas dynamical studies of both barred and non-barred spiral galaxies (see e.g., Few et al. 2016; Fragkoudi et al. 2016). Gas dynamics in `RAMSES` are simulated using a second-order unsplit Godunov scheme and an adaptive mesh refinement technique. In our models, the maximum achieved resolution is ≈10 pc, much higher than in Athanassoula (1992b). In all cases, the gas is considered isothermal with an adiabatic index of 5/3. For each one of our five bar models (R001, R010, R153, R192, and R901) we run three simulations with sound speeds $c_s = 2\,\text{km}\,\text{s}^{-1}$, $10\,\text{km}\,\text{s}^{-1}$, and $20\,\text{km}\,\text{s}^{-1}$, respectively.

The code was tested by Pastras (2022) for the types of simulations presented in this work, specifically, for all Ferrers models with an index of $n = 1$ in Athanassoula (1992a). All responses yielded identical results to the corresponding models in Athanassoula (1992b) in terms of morphology and provided a very similar description of the dust lane shocks. The `RAMSES` responses were also compared with SPH (Gingold & Monaghan 1977; Lucy 1977) models for the Ferrers bars and for a model of NGC 7479 (Pastras et al. 2022). The main morphological features and the corresponding flows were consistent in the responses of the two codes. Differences observed in the details of the developed morphological features, as well as the advantages and disadvantages of each code, are thoroughly discussed in Pastras (2022) and Pastras et al. (2022).

In our models, the gas responds to the potential described in Section 2 for a time, t, corresponding to approximately 15 pattern rotations. The initial gas surface density is the same as in Athanassoula (1992b), i.e., $1\,M_\odot\,\text{pc}^{-2}$. In the absence of self-gravity, as is the case for our models, this value is effectively a scaling factor.

The simulations begin with an initial growing bar phase that lasts for a time, t_f, corresponding to the time for three pattern rotations. During t_f, the mass of an axisymmetric disk with mass M_B is gradually transferred in a linear manner to the Ferrers bar component. In other words, during t_f, a potential component with a density of the form of Eq. (3), but with $a \approx b$, is transformed into a Ferrers bar in which $a > b$.

Finally, it is worth noting that while all our responses are in principle symmetric with respect to the origin, there are some slight deviations from perfect symmetry, possibly due to local hydrodynamical instabilities. While they do not affect any of the main conclusions of this work, traces of these asymmetries can be identified in the low density regions of the presented slit profiles.

2.3. Stellar dynamics

One of our objectives is the identification of all factors influencing the eventual shapes of the structures in the innermost kiloparsec. Thus, for each model, in addition to examining how the gas responds to the imposed potential, we conducted an orbital analysis following the procedures outlined in Athanassoula (1992a). These calculations were performed in the frame of reference that rotates with Ω_B. The equations of motion are derived from the Hamiltonian,

$$H = \frac{1}{2}\left(\dot{x}^2 + \dot{y}^2\right) + \Phi(x,y) - \frac{1}{2}\Omega_B^2\left(x^2 + y^2\right), \tag{5}$$

where (x, y) are the coordinates in a Cartesian frame of reference corotating with the bar, with angular velocity Ω_B. $\Phi(x, y)$ is the

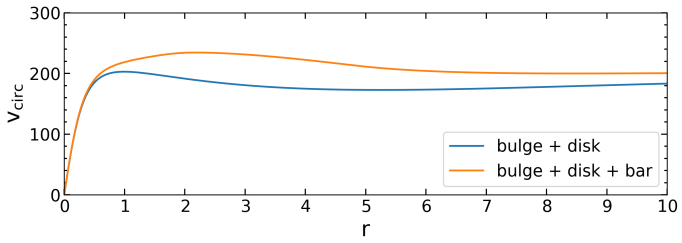

Fig. 1. Model R001: Rotation curve. The blue curve corresponds to the axisymmetric part of the potential, while the orange one to the full potential.

potential (see Sect. 2) in Cartesian coordinates, E_J is the numerical value of the Jacobian integral, and dots denote time derivatives. The unit of E_J is 1 km^2 s^{-2}. For the integration of the orbits we used a fourth-order Runge-Kutta integration scheme with a variable step. Furthermore, when necessary, we assessed the stability of the periodic orbits by analyzing the variation in Hénon's index, as described in Hénon (1965).

In our work, the location of the ILR resonance region is crucial, since it defines the domain of what we call the "x2-flow"[1]. We associate the positions of the iILR and oILR with the range spanned by the innermost and outermost periodic orbits within the x2-x3 loop in the characteristic diagrams or in Hénon's stability diagrams (see Section 3.1.1), rather than with radii derived from frequency curves for a given pattern speed, based on the axisymmetric component of the potential, or with any other alternative definition of an ILR radius (but see also Regan & Teuben 2003).

Stellar response models were also implemented by adopting a procedure akin to that used for the gaseous models. As for the latter, starting from a purely axisymmetric background, we incremented the perturbation until the desired strength was reached. Subsequently, we continued integrating the initial conditions for a duration corresponding to an additional ten pattern rotations. These stellar models are useful as they offer insights into the orbital families that ultimately become populated.

3. Results

3.1. Model R001 – The fiducial case

We use model R001, which corresponds to RUN 1 in Athanassoula (1992a), as our fiducial model. The rotation curve of the model is given in Fig. 1.

The curve representing the axisymmetric component of the potential is shown in blue, while the angle-averaged total rotation curve is illustrated in orange. This rotation curve is characteristic of a typical disk galaxy.

3.1.1. Model R001 – Orbital dynamics

The primary orbital characteristics of this model have been presented in detail in Athanassoula (1992a). In this context, we highlight specific aspects that are crucial for comprehending the dynamics of the gas within the innermost 1 kpc region.

[1] Note that orbits in the ILR region must have the appropriate Jacobi constants in order to belong to the x2-flow.

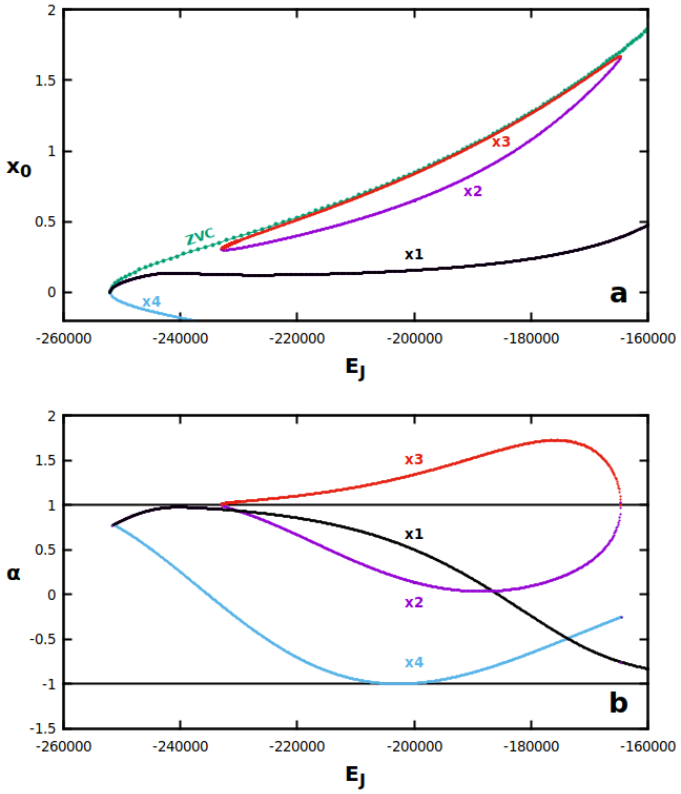

Fig. 2. Model R001: (a) Characteristic diagrams for the x1, x2 and x4 families. The zero velocity curve is depicted with a green color and indicated with "ZVC." (b) Hénon index, α, for the same families. We find no changes in the stability of any of these families.

Within the central region of this model, we only encounter x1, x2-x3, and x4 orbits[2]. The characteristic diagrams (see Sect. 2.4.4 of Contopoulos 2002) of these families for Jacobi constants, E_J, ranging from the center of the system up to the oILR of the model, are depicted in Fig. 2a. The existing families are indicated with labels with the same color as the corresponding characteristic curves, while the zero velocity curve (ZVC) for $x > 0$ is also given with a dotted green line.

The Hénon indices of the same families in the same E_J range are given in Fig. 2b. The stability of the families remains unchanged within this energy interval. Although there is a local maximum on the x1 stability curve at $(-240800, 0.97)$, there is no intersection or tangency with the $\alpha = 1$ axis. Consequently, the x1 and x2 families do not give rise to bifurcating families within the system. Also, the tangency of the x4 stability curve with the $\alpha = -1$ axis at approximately -202900 is not expected to significantly influence the local or global dynamics of the system, as it corresponds to retrograde periodic orbits, not populated in the model.

Essentially there is no chaos at the innermost kiloparsec region of the model. A typical $(x, \dot{x})$ surface of section (sos) for $E_J < E_J$(iILR) is shown in Fig. 3. In this representation, practically we can exclusively identify invariant curves. Order also dominates in the surfaces of section for E_J(iILR) $< E_J <$ E_J(oILR) (not given in a separate figure here), featuring a third

[2] We note that this is not the general case. For instance, in some potentials derived from near-infrared observations, we might observe a complex evolution of the standard families with bifurcations in the innermost kiloparsec region, along with orbits linked to the 1:1 resonance (refer to, for example, Patsis et al. 1997).

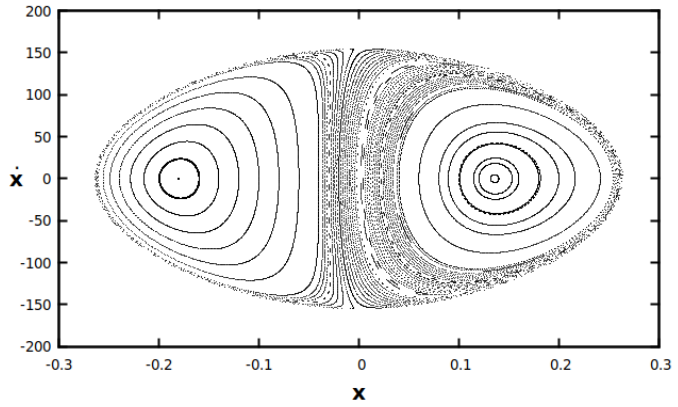

Fig. 3. Model R001: Typical surface of section for $E_J < E_J$(iILR), at $E_J = -240000$. The x4 periodic orbit is located at the center of the left stability island, while x1 is at the center of the right one.

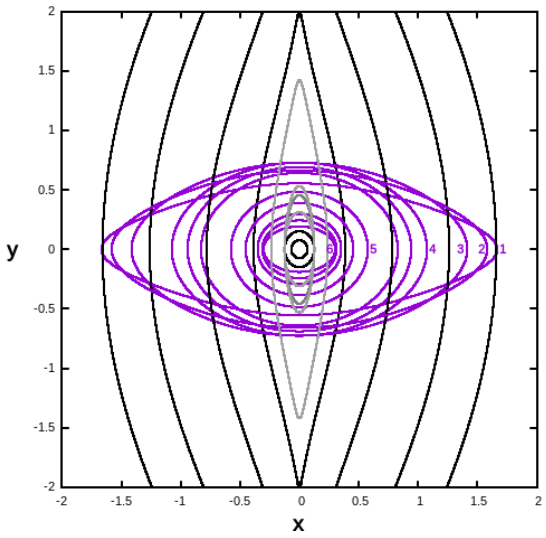

Fig. 4. Model R001: Orbits of the x1 and x2 families. The flow in our response model follows either the black x1, or the magenta x2 orbits. The gray x1 orbits exist for E_J's, where only x2 orbits are populated. The labels from "1" to "6" indicate successively the x2 orbits in descending E_J order.

stability island that emerges around x_0(x2) > x_0(x1) and negligible chaotic zones, mainly due to the presence of x3, which is situated between the boundaries of the x2 stability island and the ZVC.

The orbital background of the stellar response model is composed by the standard elliptical-like pro-grade x1 and x2 periodic orbits. In the manner in which we construct our models, beginning with circular motion in the axisymmetric background and gradually increasing the mass of the bar component (refer to Section 2.3), at each E_J, the flow is influenced by either x1 or x2 orbits. We find that the orbits populating the model are linked to the family with initial conditions closer to the circular orbits of the axisymmetric background at each E_J. The periodic orbits of these families are depicted in Fig. 4. In the plot, the x1 orbits are given in black and the x2 orbits in magenta. The orbits in gray correspond to x1 orbits that we found not to be populated, at E_J values where the flow adheres to the x2 pattern (see Section 3.1.2 below).

The outermost x1 periodic orbit in Fig. 4, occurring at $E_J = -134097.8$, being tangent to the outermost x2 orbit at $E_J = -164591.4$, is essentially the outermost elliptical-like x1 orbit of the model. This is because, for larger E_J values, the x1 orbits undergo a relatively abrupt transition to a rectangular-like shape as they approach the 4:1 resonance region. The abruptness of the transition can be understood in the increment of the x_0 initial condition of x1 from 1.66 at $E_J = -134097.8$ to 2.62 at $E_J = -130000$, pushing it well away from the x2 region (cf. with figure 2 in Athanassoula 1992a).

As is seen in Fig. 4 there is a crowding of x2 orbits in the direction of the major axis of the bar (y axis) at about 0.7 kpc, as expected (Contopoulos 1979, – figure 6). Actually there are even intersections of x2 orbits among themselves in a narrow E_J interval. In Fig. 4 the labels of the x2 orbits indicate successive periodic orbits in a descending E_J order. We find that orbit "5," for $E_J = -205000$, is the outermost x2 one that is not intersecting other members of the same family. All other x2 periodic orbits, for larger E_J, intersect other members of the x2 family.

Crowding of orbits is observed not only at the outer boundary of the x2 region, but at its inner boundary as well, as the ellipticity of the x2 orbits increases again, eventually reaching the shape of the x2 periodic orbit labeled "6". The crowding of orbits at this region is also conspicuous. For even smaller E_J than that of orbit "6", we encounter again orbits of the x1 family, of low ellipticity, which at the very central region are almost circular. Specifically, as E_J decreases to around −223000, the x1 orbits begin to resemble ellipses with low ellipticity, generally extending to sizes of $r \leq 150$ pc (Fig. 4).

The response models, during the initial transient phase, lasting for the first three pattern rotations, essentially determine which orbital families will be populated. Given that the potential variation is the same in both stellar and gaseous models, understanding the orbital families present in the stellar model helps in comprehending the flow within the corresponding regions in the gas case. This will become apparent in the subsequent sections.

3.1.2. Model R001 – Gaseous response

The morphology of the response in the central 4×4 kpc region of model R001 at time $t = 2.99$, equivalent to approximately 16.8 dynamical times (or 13.8 with the full potential) is depicted in Fig. 5. Successively, we give the responses for the models with $c_s = 2\,\mathrm{km\,s^{-1}}$ (Fig. 5a), $c_s = 10\,\mathrm{km\,s^{-1}}$ (Fig. 5b), and $c_s = 20\,\mathrm{km\,s^{-1}}$ (Fig. 5c). Clearly, we observe the development of a noticeable leading spiral feature for sound speeds of $c_s = 2\,\mathrm{km\,s^{-1}}$ and $c_s = 10\,\mathrm{km\,s^{-1}}$ (Fig. 5a and Fig. 5b, respectively).

In the $c_s = 2\,\mathrm{km\,s^{-1}}$ case, the orientation of the leading spiral arms remains consistent throughout the evolution for $t > t_f$. Two visibly open spiral arms develop from the extremities of the major axis of a central, oval-shaped, region, tilted at approximately 72° relative to the minor axis of the bar (x axis), toward its leading side. The color coding on the bottom-left side of the figures suggests that this central, oval area is a region of low surface density, significantly less dense than its immediate surroundings. The dense leading spiral arms emerge near the extremities of the major axis of this oval structure. The overall morphology is similar to that of the model without a black hole by Ann & Thakur (2005, – figure 6).

In Fig. 5b, for $c_s = 10\,\mathrm{km\,s^{-1}}$, the orientation of the oval has shifted, forming an angle of approximately 50° relative to the minor axis of the bar, once again toward the leading side of the bar. Remarkably, the pseudo-ring structure previously seen

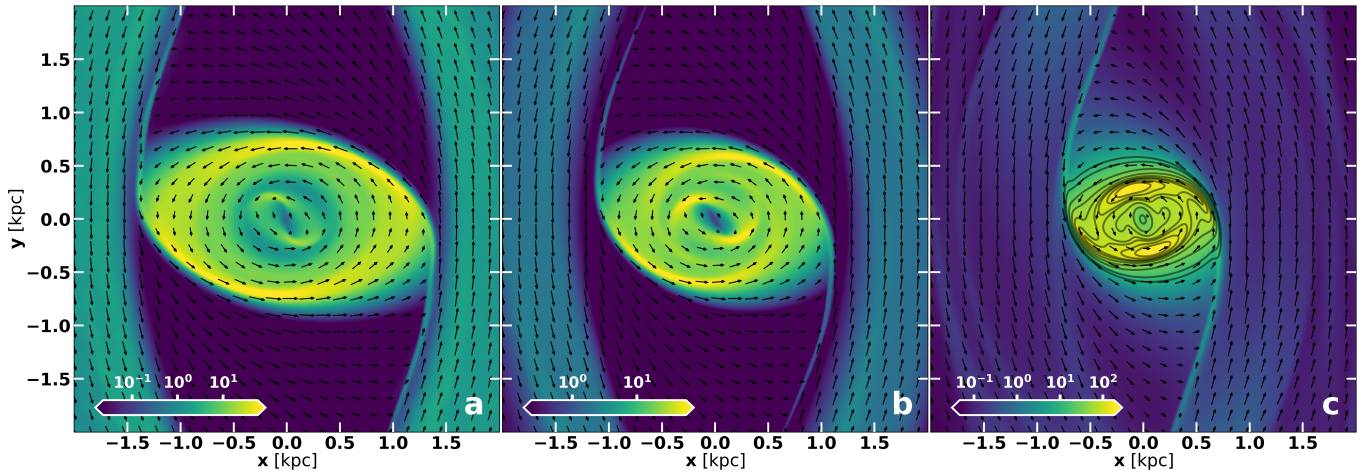

Fig. 5. Model R001: Central regions of three models with different sound speeds, (a) $c_s = 2\,\mathrm{km\,s^{-1}}$, (b) $c_s = 10\,\mathrm{km\,s^{-1}}$, and (c) $c_s = 20\,\mathrm{km\,s^{-1}}$. A leading spiral is apparent in (a) and (b), while in (c) we have the formation of a smaller pseudo-ring.

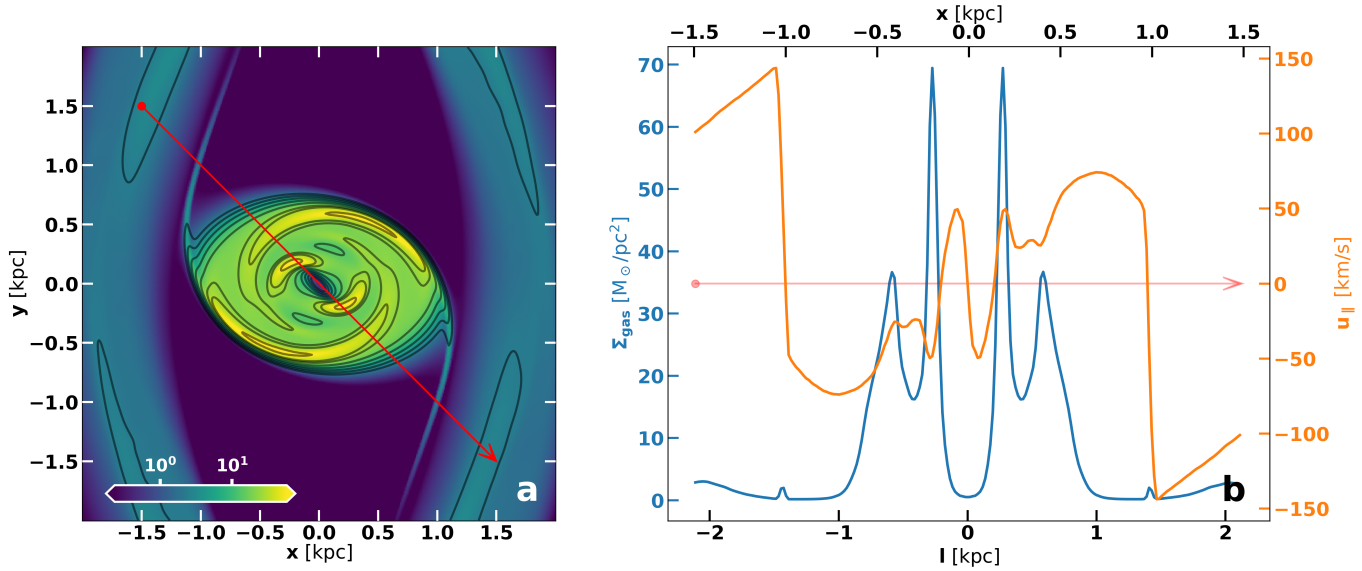

Fig. 6. Model R001: Variation in gas surface density (Σ) and the velocity component along a defined slit ($u_{\|}$) for $c_s = 10\,\mathrm{km\,s^{-1}}$. Panel (a) shows the slit's location, while panel (b) presents the variations, with the blue curve indicating Σ and the orange curve representing $u_{\|}$.

at the outer border of the x2 region in Fig. 5a with $c_s = 2\,\mathrm{km\,s^{-1}}$, has transformed into a trailing spiral pattern that extends into the area between the oILR and the iILR, gradually diminishing in the counter-clockwise direction. The transition from trailing to leading spiral arms occurs at a distance of approximately $r \approx 0.4$ from the center. In the case with $c_s = 10\,\mathrm{km\,s^{-1}}$, the prominent leading spiral arms appear broader, emerging again close to the ends of the major axis of the central, low-surface-density oval area.

We identify a spatial correlation between the clustering of orbits at the inner and outer edges of the ILR region in Fig. 4 and the dense areas (depicted in yellow) that appear at approximately the same distances from the center, but at varying angles, in the gaseous response models of Fig. 5a and Fig. 5b. The orbital crowding in Fig. 4 takes place at distances, r, $058 < r < 0.75$ (outer, along the major axis) and $r \approx 0.32$ (inner, along the minor axis). In Fig. 5a the yellow part of the pseudo-ring reaches a distance $r \approx 0.74$, while the outer tip of the leading spiral arms is at $r \approx 0.32$. In Fig. 5b the densest parts of the outer x2 region are located at $r \approx 0.72$ and the densest parts of the leading spiral arms are at $r \approx 0.3$.

In Fig. 6a, we consider a slit positioned on the snapshot depicted in Fig. 5b. This slit extends from the upper left to the lower right side of the figure, intersecting all overdense regions and traversing the system's center. It has the form of a long, red arrow, with the beginning of the slit's line segment marked with a red heavy dot. Additionally, we have overplotted isodensity curves, explicitly showing that all surface density peaks are located away from the major axis of the bar. Specifically, they emerge twisted away from the y axis, in the clockwise direction for the pseudo-ring - trailing spiral structure at the outer edge of the x2 region, and in the counter-clockwise direction for the leading spiral arms.

In Fig. 6b, the blue curve represents the variation in gas surface density along the slit. Distances are measured either along the slit starting from its beginning (given on the lower side of the figure's box) or along the x axis (given on the upper side of the figure's box). The peaks of the curve, progressing from

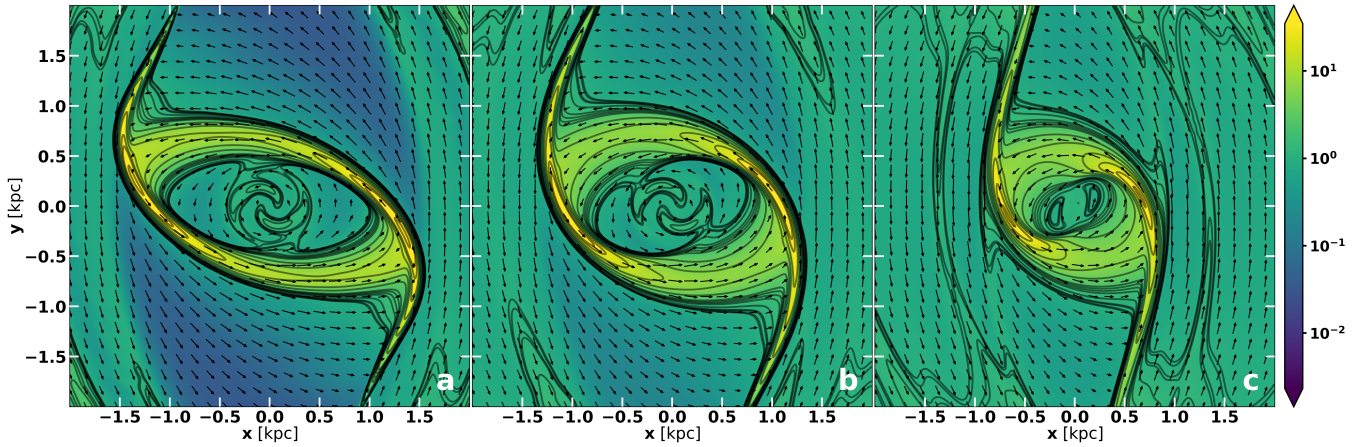

Fig. 7. Model R001: Central regions of the three models during the growing phase of the bar, with (a) $c_s = 2\,\mathrm{km\,s^{-1}}$, (b) $c_s = 10\,\mathrm{km\,s^{-1}}$, and (c) $c_s = 20\,\mathrm{km\,s^{-1}}$. The time of the snapshots corresponds to 1.7 pattern rotations after the start of the simulation.

left to right, coincide successively with distinct features: the dust lane shock (a minor peak around $x \approx -1.02$), the trailing spiral (intercepted by the slit at a point not at its maximum surface density, approximately at $x \approx -0.45$), and the leading spiral arm (at $x \approx -0.2$). Beyond $x > 0$, these local maxima reappear in a mirrored sequence. In the central region, the blue curve has a clear minimum, indicating the presence of the central oval area characterized by low surface density. The relatively empty region at the center of the model aligns with results from models with similar sound speeds by other authors (e.g., Ann & Thakur 2005).

The orange curve in Fig. 6b represents the velocity components projected onto the slit, denoted by $u_{\|}$ (given in the right-hand side of the figure's box). The curve is anti-symmetric with respect to the center of the slit. Starting from the beginning of the slit and moving from left to right, we first encounter a sharp drop in $u_{\|}$, corresponding to the minor peak of the surface density around $x \approx -1.02$ (dust-lane feature), which strongly suggests the presence of a shock. Then, as the slit enters the pseudo-ring region, $u_{\|}$ begins to rise, giving a $\Delta u_{\|} \approx 50$ close to the peak of the surface density of the trailing spiral along the slit around $x \approx -0.45$.

Subsequently, as we move along the slit toward the leading spiral arms, $u_{\|}$ drops and then has a local minimum at the local peak of the surface density within the leading arm. We note a $\Delta u_{\|} \approx 100$ from $u_{\|} \approx -50$ for $x \approx -0.2$, to $u_{\|} \approx 50$ for $x \approx -0.1$. For $x < 0$, this change in $\Delta u_{\|}$ occurs as $u_{\|}$ transitions from negative to positive values. Within the range $-0.2 < x < 0.2$, the curve displays a sinusoidal fluctuation, with $u_{\|} = 0$ at the center of the system. Beyond this region, the curve continues in a manner consistent with its anti-symmetric nature.

In contrast to the morphologies depicted in Figs. 5a,b, the case with $c_s = 20\,\mathrm{km\,s^{-1}}$ lacks a discernible central leading spiral feature (Fig. 5c). We can observe only a tendency for one of the innermost isodensity contours to form a leading structure. Apart from the absence of the leading spiral, the pseudo-ring structure appears shrinked, extending approximately to $x_{\max} \approx 0.65$ in the x direction and to $y_{\max} \approx 0.4$ in the y direction.

Noticeably, the crest of the pseudo-ring displays a set of two distinct local surface density peaks. This is visible in Fig. 5c, where we have superimposed characteristic isodensity curves in the central area of the model. The set forms roughly along the major axis of the central, low density, oval, exhibiting two local surface density enhancements. The location and structure of these enhancements is reminiscent of the "twin peaks" feature encountered in the CO emission in the central region of barred galaxies such as NGC 3351 or NGC 6951 (Kenney et al. 1992). Additionally, it is worth noting that the pseudo-ring appears to be inclined in the opposite direction, with respect to the minor axis of the system, compared to the pseudo-rings observed in the $c_s = 2$ and $10\,\mathrm{km\,s^{-1}}$ cases. However, this pseudo-ring area is located within a green-blueish region of lower, though not zero, surface density, bordered by the two dust-lane shocks and extending up to $|y| \approx 1.5$. Due to the presence of this region of lower surface density, in Fig. 5c the density outside the pseudo-ring area does not experience a sudden decline, in contrast to the cases depicted in Fig. 5a,b.

By comparing the response models shown in Fig. 5a,b,c, it becomes evident that pseudo-ring structures are consistently embedded within a "cloud" of low surface density (depicted in green-blue hues). This cloud encircles the pseudo-rings and extends toward the line segments due to the dust-lane shocks close to the x2 region, i.e., the region in which a nuclear ring-like structure is formed. Both the width of this region and its inclination relative to the bar's minor axis increase as the sound speed rises, as seen in the progression from Fig. 5a to Fig. 5c. We can say that while the cloud rotates clockwise, the pseudo-ring rotates counterclockwise and shrinks.

In Fig. 5a, with $c_s = 2\,\mathrm{km\,s^{-1}}$ the x2 region reaches a distance $|x| \approx 1.4$, slightly smaller than the extent of the largest x2 periodic orbit of the model. In Fig. 5b, with $c_s = 10\,\mathrm{km\,s^{-1}}$ the ring has shrunk, extending up to $|x| \approx 1$, while in the model with $c_s = 20\,\mathrm{km\,s^{-1}}$ (Fig. 5c) the pseudo-ring structure is confined within a maximum $|x| \approx 0.65$.

To determine the formation time of the leading spiral feature, we investigated the initial phases of the model, specifically by studying its behavior during the growing phase. The response after 1.7 pattern rotations, for the three cases with different sound speeds, is given in Fig. 7. A clearly discernible weak leading spiral emerges in the cases of $c_s = 2$ and $10\,\mathrm{km\,s^{-1}}$ (Fig. 7a and Fig. 7b). In Fig. 7a the arms almost reach the ring, while in Fig. 7b the faint leading spiral is confined within a smaller radius. At any rate, for $c_s = 20\,\mathrm{km\,s^{-1}}$ (Fig. 7c) no apparent leading spiral emerges in this region during the growing phase. We only find two local density maxima squeezed at the very center of the system, which might be interpreted as reminiscent of a leading structure. Nonetheless, even this is a transient feature.

The fact is that, in all cases, ultimately, following the conclusions drawn from the growth phase, the response to the bar

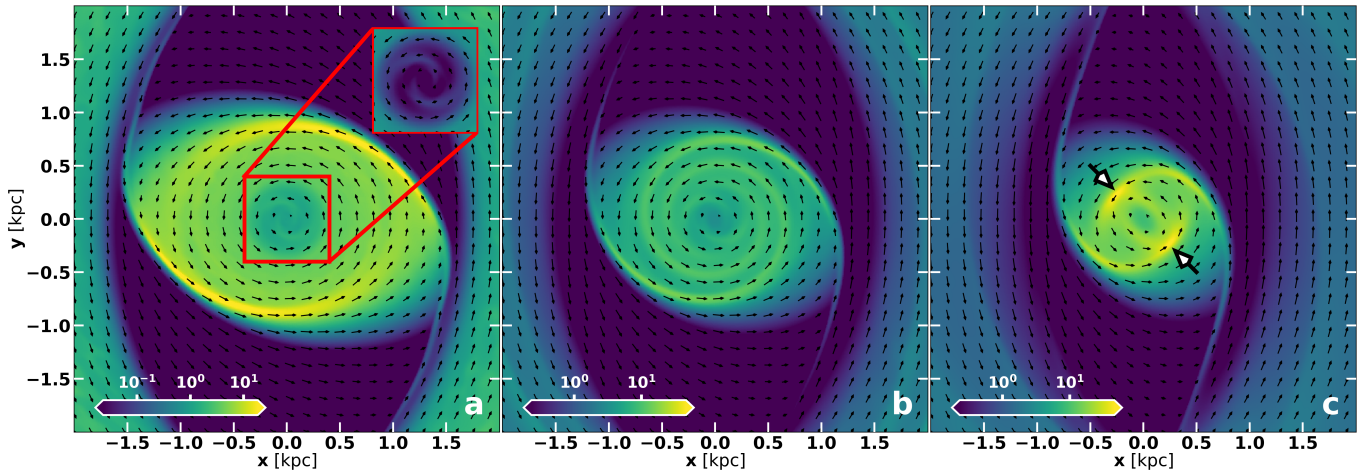

Fig. 8. Model R010: Central regions of three models with different sound speeds, (a) $c_s = 2\,\mathrm{km\,s^{-1}}$, (b) $c_s = 10\,\mathrm{km\,s^{-1}}$, and (c) $c_s = 20\,\mathrm{km\,s^{-1}}$. In (a) we give, in an embedded frame, the faint leading spiral with higher contrast. As in Fig. 5 all discussed features are embedded within an oval region, the inclination of which, with respect to the x axis, increases with sound speed.

potential with full amplitude results in the development of the ring-like structures observed in Fig. 5 for each model. The morphologies shown in Fig. 5 are already present during the growth phase and become fully established approximately 1–2 dynamical times after the bar growth is complete.

Summarizing the main findings of our study of the R001 model, we can say that:

- The emergence of the leading spiral feature is not exclusively dependent on the underlying gravitational potential. In model R001 we find it for $c_s = 2$ and $10\,\mathrm{km\,s^{-1}}$, but not for $20\,\mathrm{km\,s^{-1}}$, or at least it is so weak in the latter case that it becomes indiscernible in the gas surface density maps of our model. This already holds during the growing bar amplitude period, which lasts for three pattern rotations.
- In all three cases of model R001 with different sound speeds there is no density maximum at the center of the system. An elliptical region, with a different inclination in each of the three cases, forms at the center and always has a lower surface density than its surroundings.
- While the morphology found in the cases with $c_s = 2\,\mathrm{km\,s^{-1}}$ and $c_s = 10\,\mathrm{km\,s^{-1}}$ is rather unusual, if observed at all, in the central regions of barred galaxies, morphologies resembling that of the model with $c_s = 20\,\mathrm{km\,s^{-1}}$ are more commonly found. Examples include galaxies such as NGC 1530, which exhibit similar features as the model during the growing phase (Fig. 7c), or NGC 1433, with a morphology similar to that of the model at the end of the simulation when the full potential is considered (Fig. 5c).

3.2. Model R010 – A "round" bar

Model R010 corresponds to RUN 10 in Athanassoula (1992a). It is very similar to R001. The imposed bar is simply rounder ($a/b = 1.5$, against $a/b = 2.5$ in R001). This alteration in the topology of the bar introduces several new characteristics in the central regions of the response models. Compared to model R001, we find discrepancies in the structure of the nuclear ring and the region near the center of the system. However, these variances primarily pertain to the cooler models with $c_s = 2$ and $10\,\mathrm{km\,s^{-1}}$, whereas for $c_s = 20\,\mathrm{km\,s^{-1}}$, the deviation from R001 is minimal. The three R010 models are illustrated in Fig. 8 (compare with the corresponding models for R001 in Fig. 5).

A nuclear ring, or pseudo-ring, at the oILR region is less pronounced this time. In Fig. 8a ($c_s = 2\,\mathrm{km\,s^{-1}}$) we observe that the inclined, with respect to the minor axis of the bar, x2 oval is penetrated by the inward extension of the dust lane shocks, forming two arcs of high surface density along the periphery of the ILR region. These arcs seem to fade out quite abruptly as they tend to spiral inward in a trailing sense.

For a larger c_s, i.e., for $c_s = 10\,\mathrm{km\,s^{-1}}$ the overall morphology of the x2 region appears rounder. The shocks originating from the dust lanes continue existing as higher gas density features, penetrating the ILR region and curving inward in a spiral manner toward the center (Fig. 8b). We identify trailing spirals which reach a distance of $r \approx 200\,\mathrm{pc}$ from the center. The arm-interarm contrast is low. It is hard to say if these spiral arms are logarithmic with a very small pitch angle, or Archimedean[3]. This bisymmetric trailing spiral can be traced also in the $c_s = 2\,\mathrm{km\,s^{-1}}$ R010 model. However, its very low amplitude makes it difficult to discern clearly by eye.

We note that tightly wound bisymmetric spirals of a similar morphology are encountered throughout the entire disk (beyond the ILR region) in stellar and gaseous models responding to weak spiral potentials (Patsis et al. 1991; Patsis & Hiotelis 1994). In those cases the x1 periodic orbits supporting the spiral arms are almost circular. These works suggest that small disturbances to an axisymmetric background in spiral galaxy models cause nearly circular stable periodic orbits to be populated, offering the background support for the emergence of tightly wound (of Sa type) stellar spiral arms and gaseous arms in the corresponding hydrodynamic response models. We will see below that imposed "round" and weak perturbations are associated with tightly wound spirals in the response models.

In the $c_s = 20\,\mathrm{km\,s^{-1}}$ case (Fig. 8c), the presence of trailing spirals in the x2 region persists, yet they are of a grand-design character and terminate suddenly, giving rise to two localized surface density peaks (indicated with heavy arrows). Also in this case we have a morphology reminiscent of "twin peaks" featured in Kenney et al. (1992). There is again a central low-density region, which takes on an oval shape, akin to the warm R001 model. Although the behavior of the warm R010 model

[3] The Archimedean spiral has the property that any ray from the origin intersects successive turnings of the spiral at points with a constant separation distance.

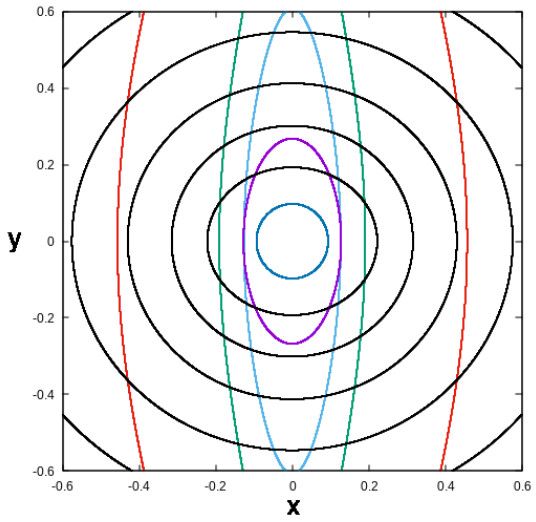

Fig. 9. Model R010: x1 and x2 orbits in the central 1.2×1.2 kpc region. The x1 periodic orbits are given with colors, while the x2 in black. The almost circular shape of the orbits is associated with the trailing spirals appearing in the gas responses in Fig. 8a,b.

bears a general resemblance to that of R001, the pseudo-ring structure, if present at all, is much weaker and less well defined (cf. Fig. 8c and Fig. 5c).

Upon careful examination of the central regions depicted in Fig. 8 for the three R010 models, it becomes apparent that the centers of these models exhibit lower densities compared to their surroundings. In Fig. 8a (with $c_s = 2\,\mathrm{km\,s^{-1}}$), a rather circular, disk-like region with a radius of approximately 400 pc is formed. The density within this region is notably lower than that of the surrounding x2 region, as indicated by the color bar at the bottom-left side of the frame. Within this disk, a leading spiral feature emerges, reaching an innermost distance from the center of about 8 pc. This feature is faint, and thus, for clarity, we also provide a frame with higher contrast embedded in Fig. 8a.

In Fig. 8b (with $c_s = 10\,\mathrm{km\,s^{-1}}$), the dominant trailing spiral within the x2 region extends to an innermost distance from the center of approximately 300 pc. At this distance, the winding direction of the bisymmetric spiral reverses, and a faint leading spiral is formed, also in this case (not readily visible in Fig. 8b). The darker color of the region very close to the center once again indicates a lower central density compared to its surroundings.

Investigating the orbital dynamics of the system, we realize that the area between the center of the system and the iILR is again dominated by order. There is no trace of chaos and the only families of periodic orbits existing in the region are x1, x2 and x3.

However, the details of the shape of the orbits in the R010 case differ from those of R001. Except for the outermost x2 orbit at $E_J \approx -160000$, all other x2 orbits are almost circular. The difference is evident in Fig. 9, which depicts the periodic orbits of the x1 and x2 families at the central 1.2×1.2 kpc (compare with the periodic orbits in the corresponding region of model R001 in Fig. 4). The almost circular shape of the x2 orbits is reflected in the formation of the tightly wound spirals in Fig. 8b, with $c_s = 10\,\mathrm{km\,s^{-1}}$. This spiral pattern is also present in Fig. 8a, albeit with a significantly reduced amplitude, making it much less noticeable. However, this correspondence to the orbital background of the model is lost when we follow the response with $c_s = 20\,\mathrm{km\,s^{-1}}$ (Fig. 8c).

The main findings of our study of the R010 case are the following:

- Model R010 indicates that round bars with an axis ratio of $a/b = 1.5$ encounter challenges in generating nuclear rings at the periphery of the x2 region akin to the one illustrated in Fig. 5 for R001.
- There is a trend toward the emergence of trailing, tightly wound nuclear spirals within the x2 region of the model. In cases where these spirals form, they eventually evolve into a leading, bisymmetric spiral structure, which prevents them from extending into the centralmost region of the system.
- The case with $c_s = 20\,\mathrm{km\,s^{-1}}$ exhibits a response similar to that of the corresponding R001 case. However, we highlight the absence of a clearly defined nuclear ring.

3.3. Model R153 – A bar without "ILRs"

Model R153 corresponds to RUN 153 in Athanassoula (1992a). It has a very fast rotating bar, which brings r_L at 3 kpc. Due to the high value of $\Omega_B = 77.726\,\mathrm{km\,s^{-1}\,kpc^{-1}}$, the locations of the resonances are considerably displaced with respect to the former cases. The whole extent of the response bar, identified by the extent of the longest x1 periodic orbit, reaches a distance $y_{\max} \approx 2.4$ kpc along its major axis. There is no ILR in this model. In the axisymmetric case, Ω_B is above the $\Omega - \kappa/2$ curve and the orbital analysis shows the absence of a x2-x3 loop in the characteristic diagram.

The gaseous responses of the R153 model for the three distinct sound speeds we examined are illustrated in Fig. 10. The presented results are contained within a 4×4 kpc box, covering nearly the entire bar region. In the absence of a x2-flow, we find a lack of rings or pseudo-rings in the system. Instead, the gaseous responses are characterized by the emergence of a multiarmed spiral structure, which becomes more pronounced with higher sound speeds. In Fig. 10c, with $c_s = 20\,\mathrm{km\,s^{-1}}$, a conspicuous fourfold spiral pattern is noticeable. The arms of this spiral pattern reach the outer regions of the bar. Meanwhile, the central area is marked by a low-density oval, which remains unaffected by the multiarmed spiral. In Fig. 10b ($c_s = 10\,\mathrm{km\,s^{-1}}$), only the outer segments of the arms are distinguishable, whereas in Fig. 10a with $c_s = 2\,\mathrm{km\,s^{-1}}$, only two spiral arm tips, tangential to the bar's oval boundary, are visible. In this latter case, within the bar region, spiral arms are scarcely found in the model's bar area. It is worth mentioning that multi-spiral responses have been previously identified by other authors, emerging from nested sequences of streamlines within regions governed by low eccentricity x1 periodic orbits in the underlying potential, as demonstrated by Sormani et al. (2015b,c – see e.g., figure 10 in Sormani et al. 2015b). However, in those instances, they are located outside the bar region, which is characterized by the presence of typical dust-lane shocks. We find something similar with the Sormani models in the overall response of our R010 model, over the whole bar and disk area.

The slit profile for the R153 model with $c_s = 20\,\mathrm{km\,s^{-1}}$ is given in Fig. 11. In Fig. 11a, the slit is depicted as a long red arrow, with its starting point indicated by a prominent red dot. The variation in surface density along the slit is depicted by the blue curve in Fig. 11b. Peaks in the curve indicate points where the slit crosses local surface density maxima, as is evident from the positions of the isodensity curves shown in Fig. 11a. Clearly the surface density decreases at distances $|x| \lessapprox 350$ pc.

The orange curve depicted in Fig. 11b demonstrates that there are no significant velocity component jumps along the slit. The discrepancies observed in the $u_{\parallel}$ component when traversing

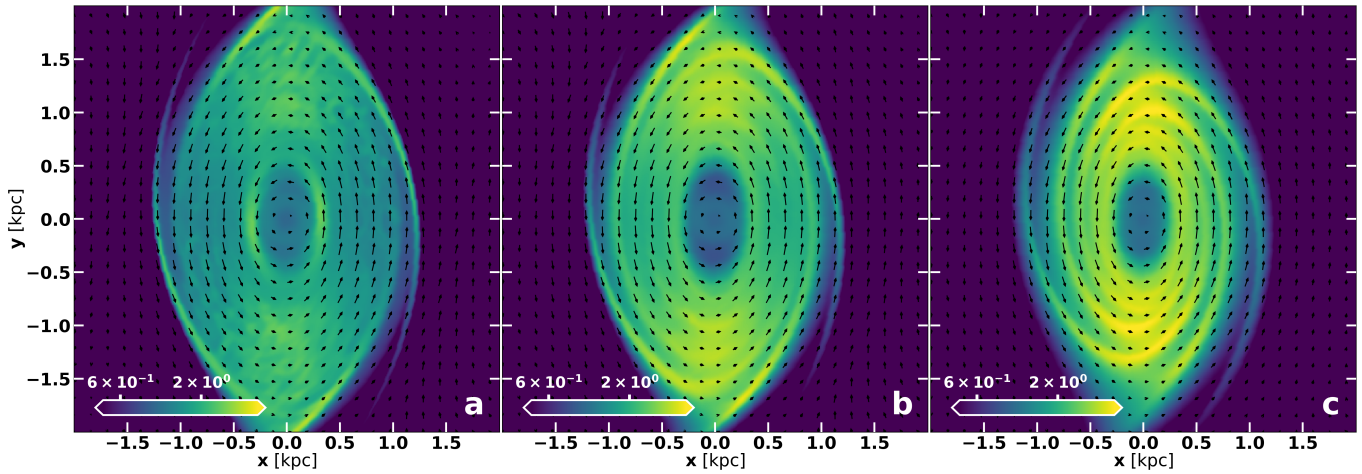

Fig. 10. Model R153: Central regions of three models with different sound speeds, (a) $c_s = 2\,\mathrm{km\,s^{-1}}$, (b) $c_s = 10\,\mathrm{km\,s^{-1}}$, and (c) $c_s = 20\,\mathrm{km\,s^{-1}}$. The responses are characterized by the presence of a multiarmed spiral structure, which becomes more pronounced with higher sound speeds.

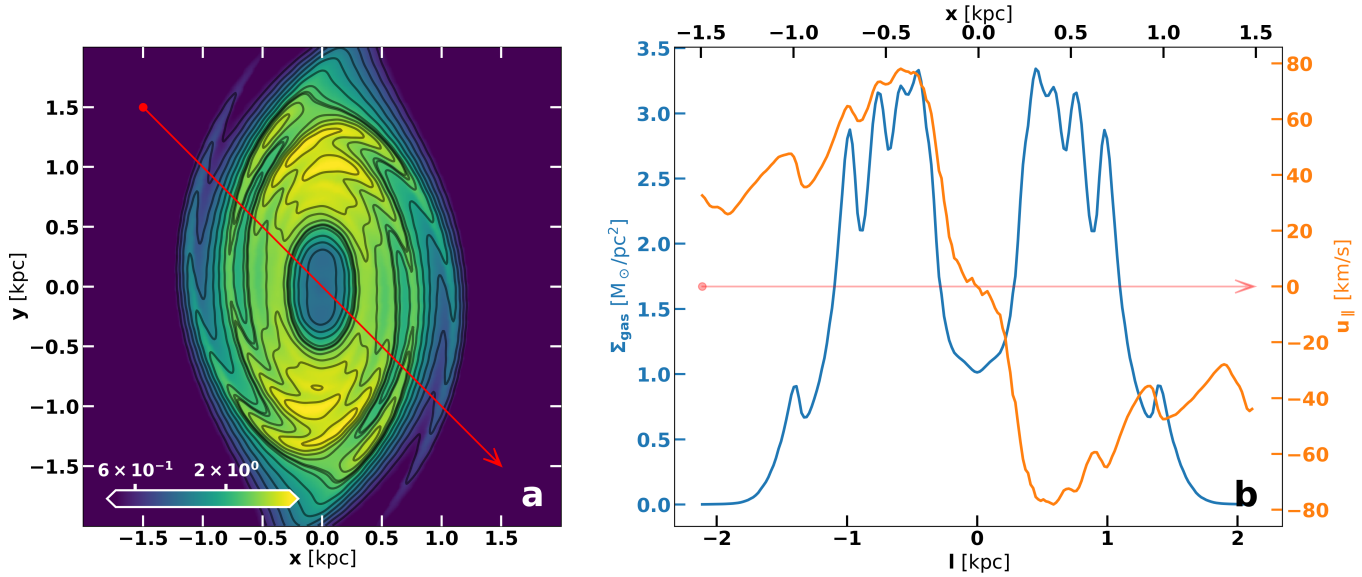

Fig. 11. Model R153: Variation in gas surface density (Σ) and the velocity component along a defined slit ($u_\parallel$) for $c_s = 20\,\mathrm{km\,s^{-1}}$. Panel (a) shows the slit's location, while panel (b) presents the variations, with the blue curve indicating Σ and the orange curve representing $u_\parallel$. The labels on the axes are the same as in Fig. 6.

the local density maxima within the spiral arm region are on the order of a few percent, while in the low-density central region, such variations are not observed at all.

Without x2 orbits present, we find only x1 periodic orbits with their major axis aligned along the major axis of the bar, extending to the center. These x1 orbits exhibit the characteristic shape of the family, and in the central region ($r \lesssim 200$), they become nearly circular (see Fig. 12). Notably, there is almost no chaos in the central bar region of the model, as evidenced by examining successive surfaces of section at the corresponding E_J values.

Model R153 exhibits a type-I gap at the 4:1 resonance (Contopoulos 1988). In this type of gap, the characteristic of the bifurcated 4:1 family lies below the x1 characteristic, in contrast to the relative positioning of the 4:1 characteristic compared to the x1 characteristic in all other models, where it is located above x1 (type-II gap) (see, for instance, model R001 in Athanassoula 1992a, figure 2). Consequently, as we approach the 4:1 resonance, we encounter periodic orbits typical for the 4:1 resonance region. The x1 orbits become diamond-like with loops, while the orbits of the 4:1 family are boxy, in alignment with the findings of Contopoulos (1988). Representatives of both families are plotted with red color in Fig. 12.

The main result of our "no-ILR" model is the absence of all morphological features in the central region resembling those we have discussed so far. We only find, as in most other models in the present work, a centrally located low-surface-density region.

The results described in this section for the response of the R153 model remain nearly identical for $\rho_c = 1.6$ (RUN 142 in the table of models in Athanassoula 1992a). This suggests that the resulting response is largely driven by the rapid rotation of the bar.

The appearance of multiarmed spirals identified within the main bar is particularly interesting. This topic will be addressed in a forthcoming paper.

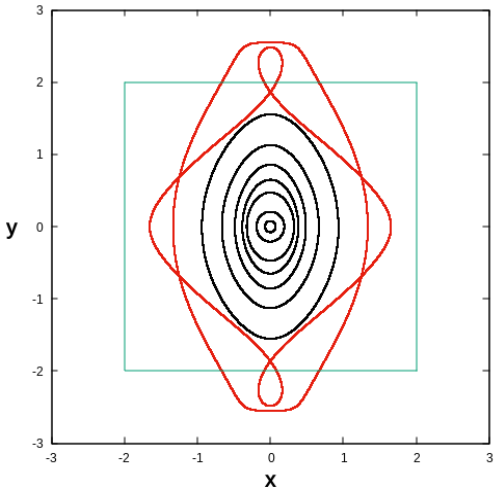

Fig. 12. Model R153: Elliptical-like periodic orbits belonging to the x1 family, spanning from the system's center up to the 4:1 resonance, depicted in black, alongside representatives of the x1 family at the 4:1 resonance region, as well as those from the 4:1 family, illustrated in red. The light blue frame outlines the region of the gaseous responses presented in Fig. 10 and Fig. 11.

3.4. Model R192 – A weak bar

Model R192 represents a weak bar model (refer to Table 1). It corresponds to the case described as RUN 192 in Athanassoula (1992a). The distinction from the reference case R001 lies in the Q_m parameter, which is set to 1.5 instead of 4.5, while the other parameters remain as in R001.

Figure 13 illustrates the response in the central region of model R192 for the three different sound speeds, as in the previous cases. Assuming a weaker bar results in a response more akin to the rounder bar of R010 than to the fiducial R001 case. Specifically, a leading spiral feature appears for $c_s = 2$ and $10\,\mathrm{km\,s^{-1}}$, but it is faint and barely noticeable. No such leading spiral feature is identified in the gaseous response for $c_s = 20\,\mathrm{km\,s^{-1}}$. The low-surface-density region in the central area of the models persists across all three cases. In Fig. 13c this region shrinks within a radius of approximately 200 pc. As with the rounder bar model, the weak bar one also shows a resemblance to the responses to weak spiral potentials presented by Patsis et al. (1991) and Patsis & Hiotelis (1994).

The case with $c_s = 20\,\mathrm{km\,s^{-1}}$ for the weak bar model R192 exhibits the longest azimuthally extended grand design trailing spiral that penetrates the x2 region, among the models studied. We emphasize the similarities between the responses to weak and round bar perturbations, as evident from the comparison between models R010 and R192.

3.5. Model R901 – A high ρ_c model

In our study, we also examined a model with parameters that were not considered in Athanassoula (1992a) (last case in Table 1). This model, R901, has a high central concentration (ρ_c is 8.3 times larger than in R001) that is reflected in the shape of the rotation curve (Fig. 14). The peak of the rotation curve for R901 has been shifted inward compared to all preceding models, now residing well within the innermost kiloparsec region, with a maximum velocity of approximately $270\,\mathrm{km\,s^{-1}}$.

The response of the R901 model for the three different sound speeds in the central 4×4 kpc box is given in Fig. 15. In this case, there are notable differences worth highlighting among the three cases. In Fig. 15a, with $c_s = 2\,\mathrm{km\,s^{-1}}$, at the outer border of the x2 region we observe the formation of a pseudo-ring. Furthermore, the progression of the dust-lane shocks from the primary body of the bar inward to the x2 region is marked by a distinct folding pattern of these shocks, preceding their convergence with the pseudo-ring. In Fig. 15b, with $c_s = 10\,\mathrm{km\,s^{-1}}$, the pseudo-ring structure is less evident; nevertheless, we can observe the emergence of a relatively circular inner disk. This disk is characterized by the formation of a faint inner trailing spiral winding toward the system's center, as one can realize by a careful inspection of the figure. The outermost part of this spiral, at $r \approx 0.8$ kpc, at the border of the x2 region, has the highest surface density along the spiral, similar to the corresponding case in R192 (Fig. 13). The difference is that in the R901 case, the inner spiral is barely discernible. Finally, in Fig. 15c, with $c_s = 20\,\mathrm{km\,s^{-1}}$, the dust-lane shocks persist inward, forming this time an inner disk with a discernible, tightly wound spiral pattern.

However, the most noticeable distinction lies in the center of each of the three models. In Fig. 15a, there is a prominent central low-density disk-like region with a radius of approximately $r \lesssim 350$ pc. In Fig. 15b, the density decreases to a lesser extent, with the color coding indicating a density minimum only at the very center. The surface density in the x2 region appears much more uniform compared to Fig. 15a. Finally, contrarily to the first two, and all previous models, in Fig. 15c the surface density seems to increase toward the center. In order to have a closer look at this model we consider again the isodensities in the central region (Fig. 16a) and the variation in the surface density and the velocity component along a slit (Fig. 16b).

In Fig. 16b, we note that the blue curve, representing the surface density variation along the slit shown in Fig. 16a, rises toward the system's center, exhibiting fluctuations corresponding to the arms of the trailing spiral observed in the x2 region. Within the innermost 45 pc, the gas density decreases by 7.8%. No evident leading spiral is observed in this case. However, in Fig. 16a, we can discern two density peaks, corresponding to the two local maxima of the blue curve near the center in Fig. 16b. Their location and structure has, as in the R001 and R010 "warm" models (Figs. 5c and 8c, respectively), a "twin peaks" character. However, in this case, in the absence of a pseudo-ring, they appear much closer to the center, where gas is accumulated. In Kenney et al. (1992) an example with "twin peaks" close to the center is given for the weakly barred galaxy (of SAB(rs)cd type) M101 (see their figures 1 and 3). The variation in the orange curve indicates that practically the only shocks happen at the loci of the dust-lane shocks outside the x2 region. We conclude that the dust-lane shocks transport gas into the already gas-rich central region, where it is further compressed into smaller radii.

To explore a potential connection between the orbital structure and the gas response, it is helpful to additionally analyze the model's orbital dynamics. The characteristic of the model is illustrated in Fig. 17. Both the x1 and x2 families coexist within the energy range $-350000 \lesssim E_J \lesssim -150000$. The stellar bar consists of orbits trapped around stable periodic orbits within this energy range. The local maximum of the x1 characteristic is at $E_j \approx -127000$. Spatially, the orbital backbone of the periodic orbits that support the bar of the model is given in Fig. 18. In close proximity to the center, for $E_J \lesssim -350000$, only almost circular x1 orbits exist, with $r \lessapprox 30$ pc. Almost circular orbits belonging to both x2 and x1 family, not intersecting other periodic orbits, are present for $r \lessapprox 300$ pc, as can be inferred by

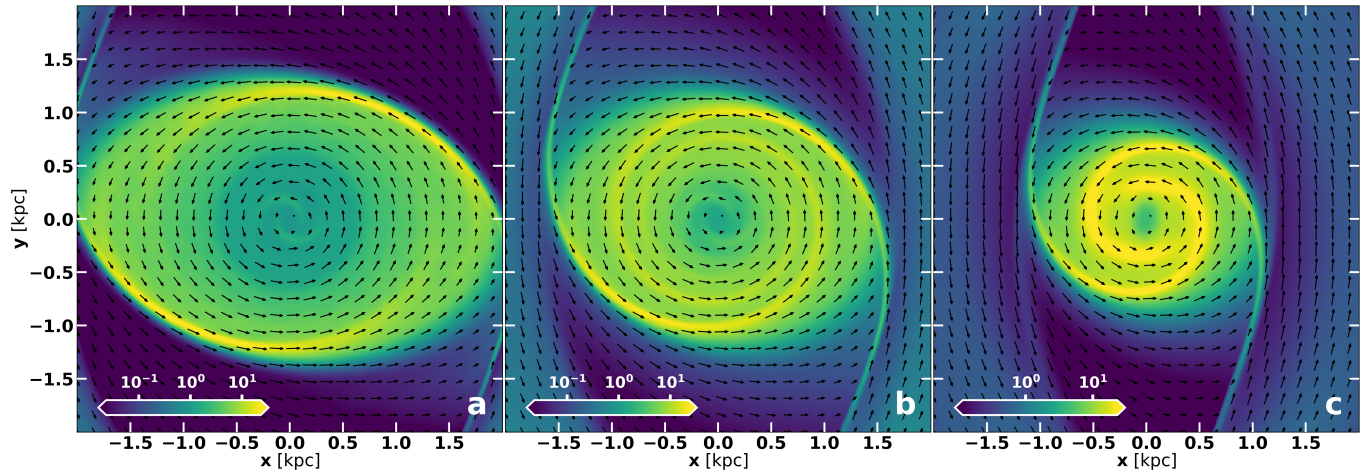

Fig. 13. Model R192: Central regions of three models with different sound speeds, (a) $c_s = 2\,\mathrm{km\,s^{-1}}$, (b) $c_s = 10\,\mathrm{km\,s^{-1}}$, and (c) $c_s = 20\,\mathrm{km\,s^{-1}}$. The model is characterized by the presence of trailing spirals in the x2 region, becoming more open with increasing sound speed.

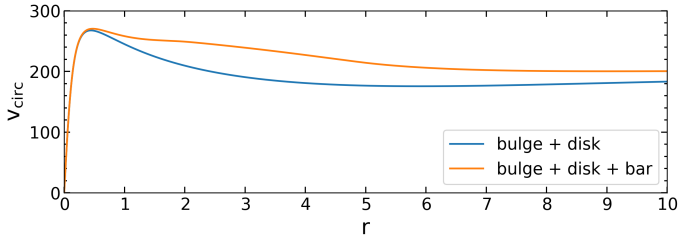

Fig. 14. Model R901: Rotation curve. The blue curve corresponds to the axisymmetric part of the potential, while the orange one to the full potential.

the inspection of the embedded zoom of the central region in the upper right corner of Fig. 18. This region corresponds to the central disk of low density observed in Fig. 15a.

The R901 model, with a sound speed of $c_s = 20\,\mathrm{km\,s^{-1}}$, is the sole model encountered thus far in our study that, in practical terms, draws the gas close to the system's center. Consequently, we next examine two models with very weak bars to gain a deeper understanding of the role of the axisymmetric background, compared with the role of the bar component, in shaping the central 1 kpc morphology.

4. Comparison with extremely weak bars

Explanations for the presence of the leading spirals, as well as for the overall morphologies appearing in the gas in the central 1 kpc region, are sought within the framework of the linear approximation (see, for example, Wada 1994; Maciejewski 2004a; Sormani et al. 2015b). However, such an approach is significantly different from that in which a firmly established bar is present. We aim to identify which characteristics of the models already emerge when gas responds to very weak barred perturbations and which require stronger perturbations to manifest. In our models, we initially have a nearly axisymmetric phase during the early stages of our simulations, but this phase is transient and occurs only during the growth phase. Thus, we investigated the response to very weak barred potentials over several pattern rotations.

We present two extremely weak bar models with sound speed $c_s = 10\,\mathrm{km\,s^{-1}}$, the parameters of which are summarized in Table 2. Upon comparing the parameters of the model labeled R801 with those of R001 in Table 1, we note a difference in Q_m, which has a value of 0.1 in the case of R801 instead of 4.5 for R001. On the other hand, R991 shares similarities with R901, featuring a high ρ_c, but differing in Q_m, which is once again 0.1 instead of 4.5. This practically makes the bulge the important component of the models. The rotation curve of R801 is close to the one of R001 and that of R991 close to that of R901 and all four models have two ILRs.

In Fig. 19 we give the overall R801 response (Fig. 19a) and the response in the central 4×4 kpc box (Fig. 19b). In Fig. 19a, we note the absence of a discernible bar component and the absence of straight-line dust-lane shocks. The figures include the velocity vectors, with the corotation region becoming apparent when considering their size and direction. Within a radius of $r < 2$ kpc, a bisymmetric spiral pattern emerges that can be better appreciated in Fig. 19b. It reaches an innermost radius of $r \approx 0.8$ kpc. The model is characterized by a central oval area with lower density than its surroundings, as in the R001 model, this time for $r \lessapprox 0.45$ kpc. However, there is no apparent leading spiral feature formed in R801.

The lack of distinct dust-lane shocks beyond the region with $r \gtrsim 2$ in R801 can be attributed to the much lower relative bar forcing, $F_{\mathrm{pert}} = F_{\mathrm{bar}}/F_{\mathrm{total}}$, in this model with respect to that of R001. In Fig. 20, we present F_{pert} for the two models discussed in this section (R801, R991), along with their corresponding models that include the full bar perturbations (R001 and R901, respectively). We find that for $2 < r < 6$, we have $0.008 < F_{\mathrm{pert}} < 0.015$ in R801 and $0.35 < F_{\mathrm{pert}} < 0.48$ for R001. This difference is also evident in the orbital structures: the weaker perturbation in R801 results in nearly circular x1 orbits, while in R001, the x1 family's periodic orbits are elliptical-like.

In the central 1 kpc region, both R801 and R001 models exhibit low relative forcing; however, it is significantly lower in R801 than in R001. Specifically, the relative forcing for R801 is $F_{\mathrm{pert}} < 0.003$, while for R001 it is $F_{\mathrm{pert}} < 0.17$. We highlight that both models have two ILRs (similar variation in their $\Omega(r) - \kappa(r)/2$ curves) and similar initial surface densities throughout their disks. Both models show a kind of trailing bisymmetric spiral in the 1 kpc region (more pronounced in the R801 case), but only R001 includes a clear leading spiral. The shapes of the three innermost isodensities in Fig. 19b suggest a tendency toward the development of a leading component; however, this

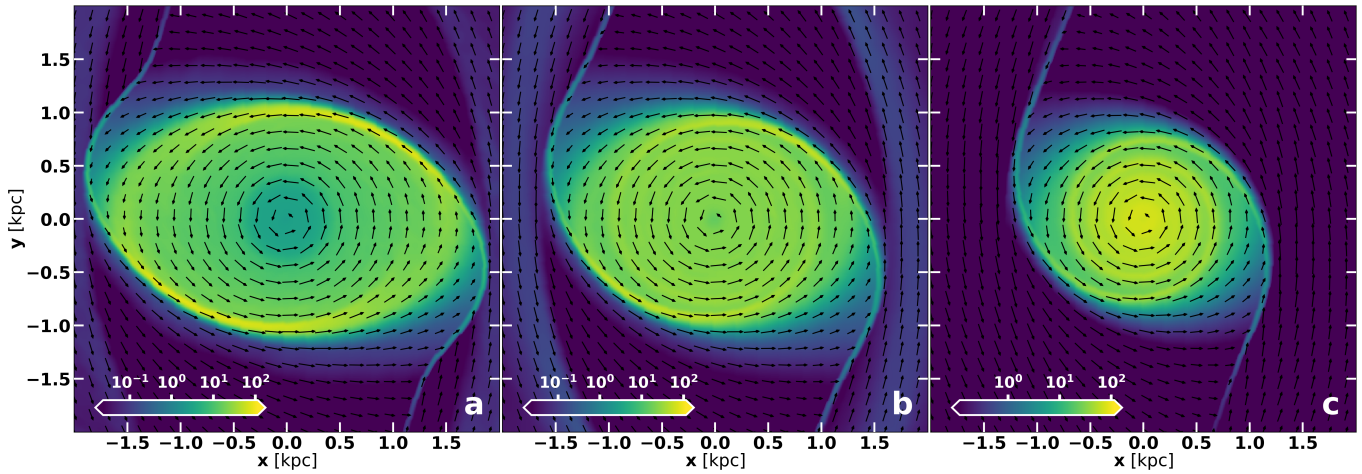

Fig. 15. Model R901: Central regions of three models with different sound speeds, (a) $c_s = 2\,\mathrm{km\,s^{-1}}$, (b) $c_s = 10\,\mathrm{km\,s^{-1}}$, and (c) $c_s = 20\,\mathrm{km\,s^{-1}}$. We find that, contrarily to all previous models, in (c) the surface density increases toward the center.

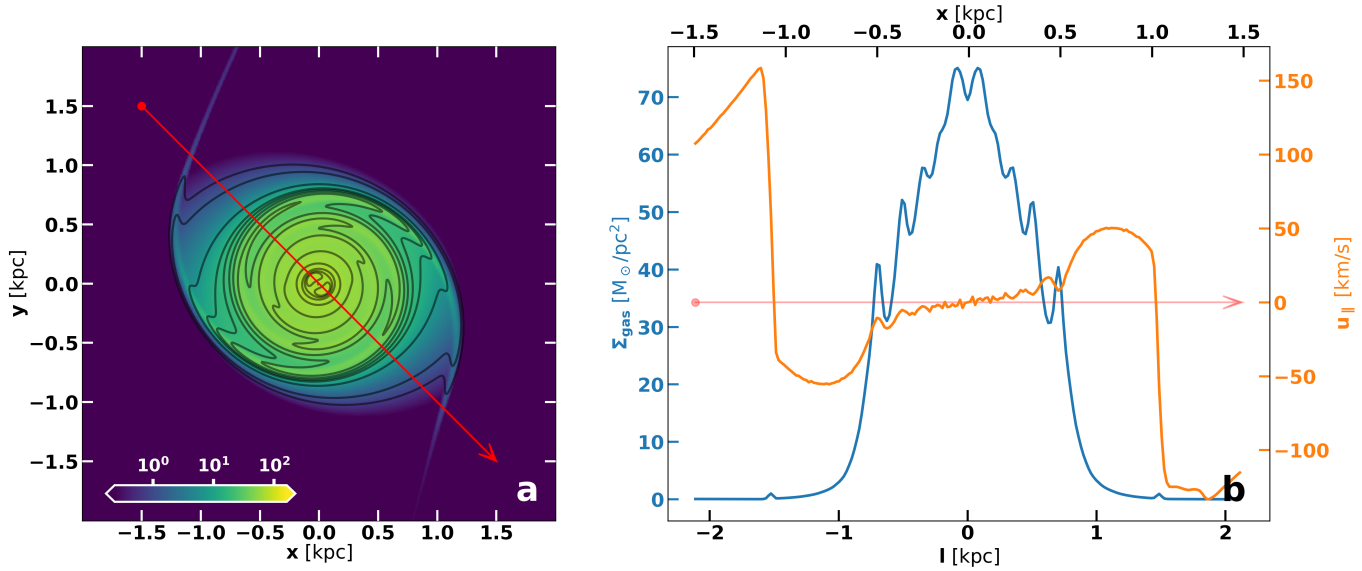

Fig. 16. Model R901: Variation in gas surface density (Σ) and the velocity component along a defined slit ($u_\parallel$) for $c_s = 20\,\mathrm{km\,s^{-1}}$. Panel (a) shows the slit's location, while panel (b) presents the variations, with the blue curve indicating Σ and the orange curve representing $u_\parallel$. The labels on the axes are the same as in Fig. 6.

remains far from forming a well-defined leading spiral feature. Since the rest of the dynamical and hydrodynamical parameters are similar, the presence of the leading spiral feature (cf. Fig. 5b and Fig. 19b) is primarily influenced by the relative forcing, which is reflected in the shape of the periodic orbits in the region.

The main distinction between the high ρ_c models R991 and R901 primarily also lies in the absence of dust-lane shocks in the main body of the bar in R991, which is nearly axisymmetric. As the center is approached in model R991, a tightly wound, trailing, bisymmetric spiral forms and becomes the dominant structure in the $2.5 \lessapprox r \lessapprox 1.3\,\mathrm{kpc}$ region (Fig. 21a). In the corresponding region of R901, dust lane shocks are present, extending up to a nuclear pseudo-ring structure. Closer to the center ($r < 1\,\mathrm{kpc}$), both models exhibit similarities, including a disk with nearly uniform density and weak spiral features. In R991, the spirals are fragmented, and the central surface density within $r < 0.1\,\mathrm{kpc}$ is higher compared to its surroundings (Fig. 21b). In contrast, for the strong bar model R901, the surface density in this region is comparable to, if not lower than, that of its surroundings (Fig. 15b). However, in absolute terms the strong bar model R901 with $c_s = 10\,\mathrm{km\,s^{-1}}$ accumulates considerably more gas in the central $r < 0.1\,\mathrm{kpc}$ region compared to R991, as expected (Fig. 22).

To gain a clearer understanding of the central spiral patterns that develop in the two very weak bar cases, we examined the variations in surface density and the velocity component along a defined slit. These variations are shown in Fig. 23a and Fig. 23b for the R801 model, and in Fig. 23c and Fig. 23d for the R991 model.

In Fig. 23a, it is evident that there is a density minimum at the central region of the R801 model. The variation in the blue curve in Fig. 23b shows that the surface density on the spiral arms (local peaks of the blue curve) decreases as we approach the center, with a near-continuous decline for $|x| \lesssim 0.5\,\mathrm{kpc}$. The $u_\parallel$ variation (orange curve) reveals that $\Delta u_\parallel$, measured where the

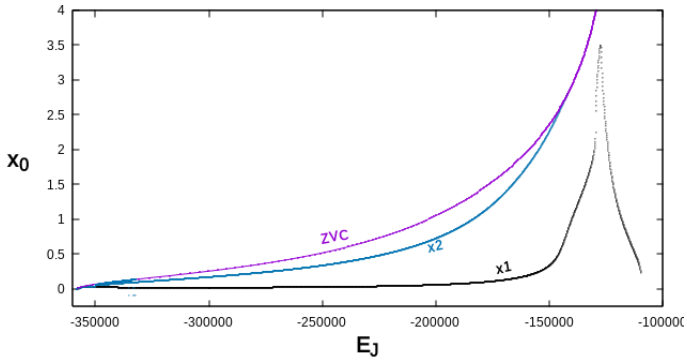

Fig. 17. Model R901: Characteristics of the main families of the model. The zero velocity curve is indicated with "ZVC" and is given in purple color.

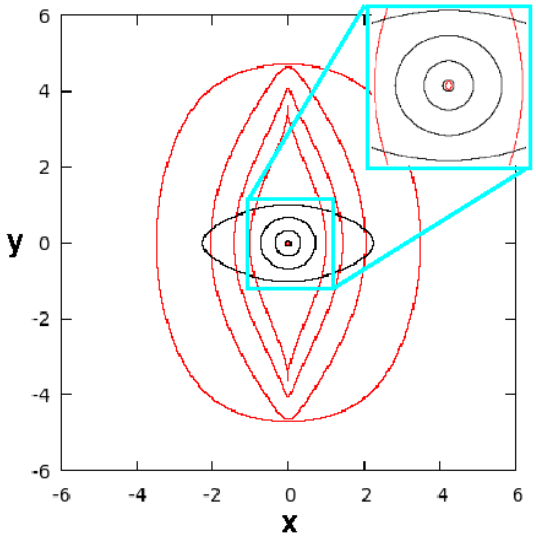

Fig. 18. Model R901: Orbital backbone of the whole bar. In the embedded frame we zoom in the central region. The x1 and x2 orbits are depicted in red and black, respectively.

Table 2. Dynamical parameters of the two extremely weak bar models.

Model	a/b	r_L	$Q_m/10^4$	$\rho_c/10^4$	Ω_B
R801	2.5	6.0	0.1	2.4	32.86
R991	2.5	6.0	0.1	20.0	33.38

slit intersects spiral arms also decreases closer to the center for $0.5 \lessapprox |x| \lessapprox 1$ kpc. Near the center, $\Delta u_{\parallel}$ shows minimal variation. At the first crossing with a spiral arm, $\Delta u_{\parallel} \lesssim 10\,\mathrm{km\,s^{-1}}$ (the extrema of the orange curve before and after the peak of the blue curve for $|x| \approx 1$), while for $|x| \lesssim 0.5$ kpc, $\Delta u_{\parallel} \lesssim 4\,\mathrm{km\,s^{-1}}$.

In Fig. 23c, we see that in the R991 model, the spiral arms formed are even more tightly wound than in R801 (Fig. 23b). The variation in the blue curve in Fig. 23d indicates that as we move along the slit toward the center, beyond the second cut with the spiral arms, there are small density fluctuations before the curve starts rising, eventually peaking very close to the center. The variation in the curve highlights the presence of faint spiral segments and a twin-peaks feature at $r \approx 68$ pc, morphologically similar to what is identified in the case of R901 with $c_s = 20\,\mathrm{km\,s^{-1}}$. The variation in $\Delta u_{\parallel}$ remains small, increases along with the surface density toward the center, exhibiting a pattern of successive rises and falls, ultimately reaching a value around $10\,\mathrm{km\,s^{-1}}$ (note the difference in scale of the $u_{\parallel}$ axes between Fig. 23d and Fig. 16b).

We conclude that in both very weak bar cases the change in the velocity parallel to the slit ($\Delta u_{\parallel}$) is small compared to the shocks in the main body of the bar. Specifically, shocks are not identified in the region within the central kiloparsec of the models. The rapid fluctuations in $u_{\parallel}$ for $|x| < 1$ correspond to the region where the gas exhibits clumpiness in R991.

In summary:

- The responses of both R801 and R991 models suggest that, while the dynamics within the main bar region reflect the influence of the imposed bar potential, the central region is strongly influenced by the hydrodynamic properties of the model. In two models with similar perturbing forces as the R801 and R991 models, if a high surface density is initially set at the center (R991), it persists throughout the simulation; without it (R801), the central density remains low, lower than in its surroundings, as in the case with the full potential.
- Some arising differences can also be attributed to variations in the relative forcing. In models with identical sound speed, the stronger perturbation in R901 transports more gas to the central region than the much weaker perturbation in R991 (Fig. 22). However, qualitatively, models with weaker perturbing forces in the x2 region, such as R991 – which fail to form nuclear or pseudo-rings – tend to accumulate more gas near the center (within 100 pc) relative to the mean density in the innermost 1 kpc compared to models with stronger perturbations, such as R901 (cf. Fig. 21b or Fig. 23c with Fig. 15b).
- The presence or absence of a conspicuous central leading spiral depends on the forcing due to the bar component, as is indicated by its apparent absence in the nearly axisymmetric R801 model, while it is a conspicuous feature in R001 (cf. Fig. 19b or Fig. 23a with Fig. 5b).

5. Discussion and conclusions

Gas accumulation in orbit-crowding regions arises from the non-axisymmetric forcing in barred potentials, which drives stellar and gaseous streamlines to converge Athanassoula (1992b). In stellar models, periodic orbit families alone predict the loci of enhanced density, but in gaseous models the sound speed, c_s, critically shapes the response. At low c_s, gas is highly compressible, so orbit crowding produces strong shocks and density enhancements that closely follow stellar predictions. At higher c_s, pressure forces redistribute the gas, weakening shocks, smoothing density contrasts, and shifting the dense lanes closer to the bar's major axis (Wada 1994; Maciejewski 2004a; Kim et al. 2012b). Thus, increasing c_s reduces gas accumulation and displaces dense structures, highlighting the growing role of pressure support in the ISM.

We carried out a series of gas response models using the classic Ferrers bar potential. In our simulations, we did not account for the self-gravity of the gas, nor did we include an explicit black hole component at the center of the model. The impact of gas self-gravity has been explicitly examined in Wada & Habe (1992) and subsequently in Wada & Habe (1995). Furthermore, Wada & Koda (2001) demonstrated that adopting a more realistic description of the interstellar medium leads to resonant structures that differ qualitatively from those obtained in simplified isothermal models. These results highlight the need for caution when interpreting sound-speed–driven effects. Nevertheless, the

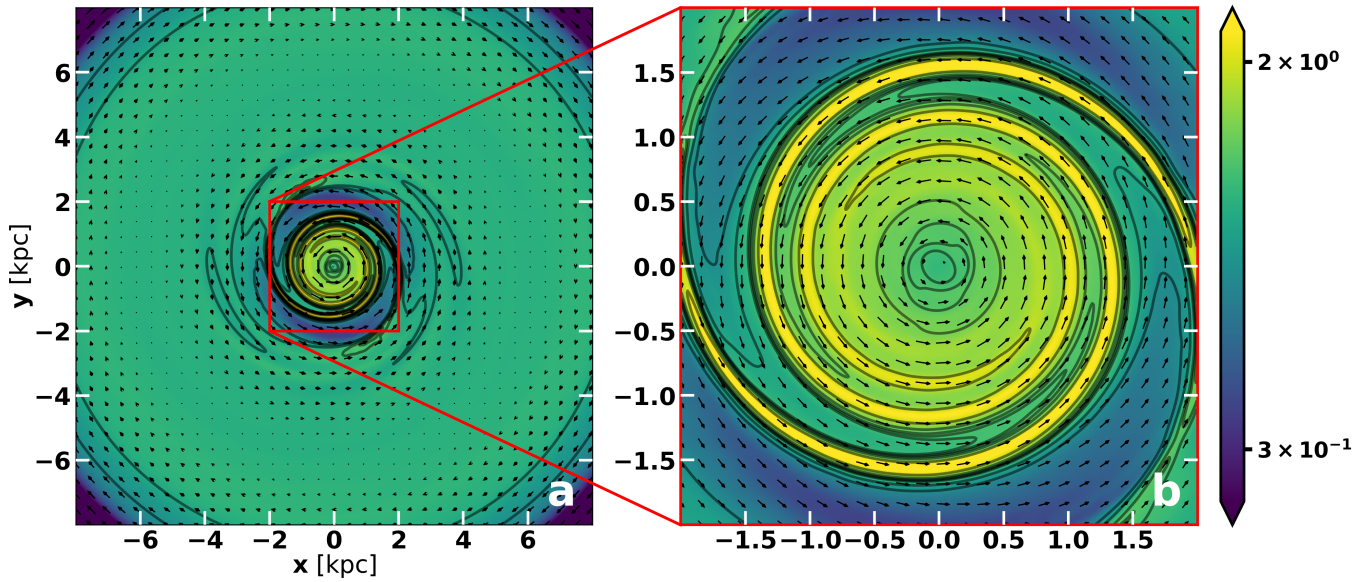

Fig. 19. Model R801: Gas response of the model with $c_s = 10\,\mathrm{km\,s^{-1}}$ in (a) 16×16 kpc frame and (b) in the central 4×4 kpc region. Apparently, the innermost 0.025 kpc have a lower surface density (greenish) compared to the yellowish surroundings and the yellow spiral arms.

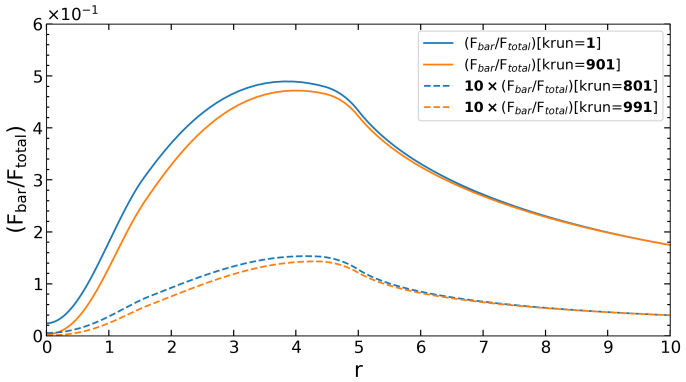

Fig. 20. Perturbing force variations for the four models R001, R801, R901, and R991.

present study does not aim to resolve the detailed thermodynamical processes, but rather to capture the general dynamical response of the gas in the central regions of bars. In this sense, our models illustrate the principal trends and indicate the direction in which variations in specific parameters influence the resulting nuclear morphologies.

As Sormani et al. (2024) indicate, the isothermal approximation should not be interpreted literally, but rather as an effective description that compresses a variety of complex physical processes into a single tunable parameter. In this sense, the adopted sound speed does not measure the true kinetic temperature of the gas; instead, it acts as an "effective temperature" that crudely averages over the multiphase structure of the interstellar medium, the influence of unresolved turbulent motions, and additional forms of pressure support, such as magnetic fields. While this treatment is clearly idealized, its strength lies in the ability to capture, in a controllable and transparent manner, the global dynamical trends of gaseous flows in barred galaxies. Comparisons with more detailed simulations indicate that the essential mechanism leading to nuclear ring and spiral formation is robust and can be adequately reproduced within this simplified framework.

Based on these assumptions, we draw the following conclusions:

1. In all the cases we examined, nuclear rings or nuclear spirals were present, with the exception of model R153, which lacked inner Lindblad resonances. This leads to the conclusion that the formation of nuclear substructures within galactic bars is consistently associated with the presence of an ILR (x2) region. Models without x2-flows do not have nuclear rings, or spirals, in good agreement with what was found by Athanassoula (1992b).
2. In images of galaxies, the observed nuclear rings are either round, as in the case of NGC 1097, or (in most cases) rather mildly elongated, as for NGC 6951 or NGC 1433. In our models we encounter nuclear rings of different shapes. The elongation of the nuclear ring, which is approximately aligned along the minor axis of the bar, decreases with increasing sound speed. The most well-defined nuclear rings are identified in the cases with $c_s = 2\,\mathrm{km\,s^{-1}}$, for all models in our study. However, their elongation appears somewhat larger than what is in general observed in real galaxies. At $c_s = 10\,\mathrm{km\,s^{-1}}$, only pseudo-rings are evident, while at $c_s = 20\,\mathrm{km\,s^{-1}}$, the ring structures, if present, as in the fiducial model R001, are smaller and rounder than in the two previous cases. In warm models in which they do not form, we find nuclear trailing spirals directly connected to the relatively straight dust lanes associated with the large-scale bar, in agreement with observations of galaxies such as NGC 1530. This morphology is predominantly identified in models with an effective sound speed of $c_s = 20\,\mathrm{km\,s^{-1}}$.
3. We find two kinds of nuclear trailing spirals in our models: those encountered in models with $c_s = 20\,\mathrm{km\,s^{-1}}$ (R010 and R192), which can be described as grand design, terminating in a region of low surface density, and those in models with $c_s = 10\,\mathrm{km\,s^{-1}}$ (R010, R192, R901, R801, and R991), which are tightly wound and extend azimuthally more than 2π. A particular case is the high ρ_c, warm model R901, in which

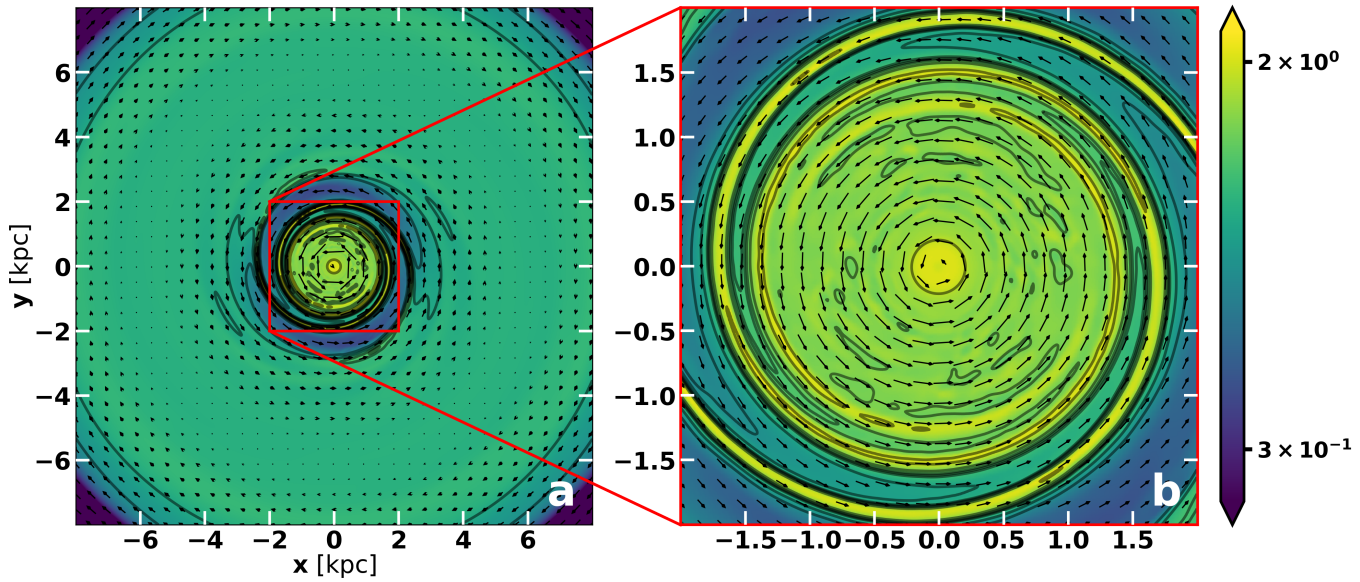

Fig. 21. Model R991: Gas response of the model with $c_s = 10\,\mathrm{km\,s^{-1}}$ in (a) 16×16 kpc frame and (b) in the central 4×4 kpc region. The innermost 0.025 kpc have a higher surface density (yellow) compared to the surrounding region (greenish).

a tightly wound, trailing spiral is formed, terminating in a featureless inner disk. Tightly wound spirals are more distinct in weak perturbation models (R192, R801, and R991) and less so in models with strong perturbing forces (R010 and R901). Comparing the responses of the same model but with different sound speeds, we find that the nuclear spirals become more open, i.e., their pitch angle increases, as the sound speed increases. Typical cases are models R010 and R192, in which we have tightly wound nuclear spirals for $c_s = 10\,\mathrm{km\,s^{-1}}$ and open grand design patterns for $c_s = 20\,\mathrm{km\,s^{-1}}$. Notably, weaker bars and nearly axisymmetric models tend to host such spirals. This is in agreement with the results of Maciejewski (2004b) and with the observations of Martini et al. (2003a,b). It is also consistent with the improved self-consistency of tightly wound spirals when modeled under weak perturbations, as described by Patsis et al. (1991) and well reproduced in SPH simulations (Patsis & Hiotelis 1994).

4. Nuclear spirals directly connected to the relatively straight dust lanes associated with the large-scale bar, which are observed in galaxies such as NGC 1530, are predominantly found in models with $c_s = 20\,\mathrm{km\,s^{-1}}$. This does not imply that x2-flows are absent in the corresponding stellar models. Similar morphologies are also present in the weaker bar model R192 and the round bar model R010, with $c_s = 10\,\mathrm{km\,s^{-1}}$. However, in both of these cases the nuclear spirals are tightly wound.
5. When a well-defined nuclear ring fails to form, tightly wound trailing spirals emerge within the ILR region. These spirals appear as grand design structures in warm gas models (R001, R010, R192, and R901), while in models with $c_s = 10\,\mathrm{km\,s^{-1}}$ (R010, R192, R901, R801, and R991) they are tightly wound. These latter spirals do not reach the system's center but terminate in a region of low surface density (R010 and R192) or a featureless inner disk, which dominates the innermost 1 kpc region (R901, R801, and R991). They are more distinct in weak perturbation models (R192, R801, and R991) and less so in models with strong perturbing forces (R010 and R901).

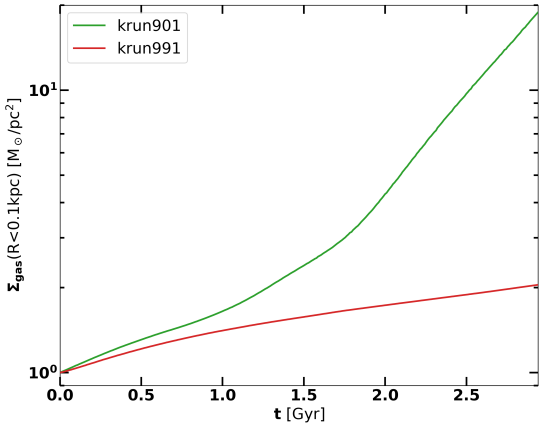

Fig. 22. Surface density evolution in the central $r < 0.1$ kpc region for models R901 and R991. We find that the R901 model accumulates an order of magnitude more gas in the central region than the almost axisymmetric model R991.

6. Several studies have proposed mechanisms for the formation of leading spiral segments in barred galaxies under specific resonance and orbital precession conditions. In general, when two ILRs are present, the precession rate $\Omega - \kappa/2$ decreases toward the center, generating leading nuclear spirals at the iILR due to the positive torques exerted by the bar (Combes 2002, 2022). The presence of a massive central component, most effectively the presence of a black hole, alters the shape of $\Omega - \kappa/2$, making it increase monotonically toward the center and preventing the formation of a leading spiral. Wada (1994) provided an analytic model for non-self-gravitating gas in a weak bar potential, showing that damped elliptical orbits driven by periodic forcing can produce leading or trailing spiral-like enhancements near the first and second ILR, respectively. These results indicate that leading

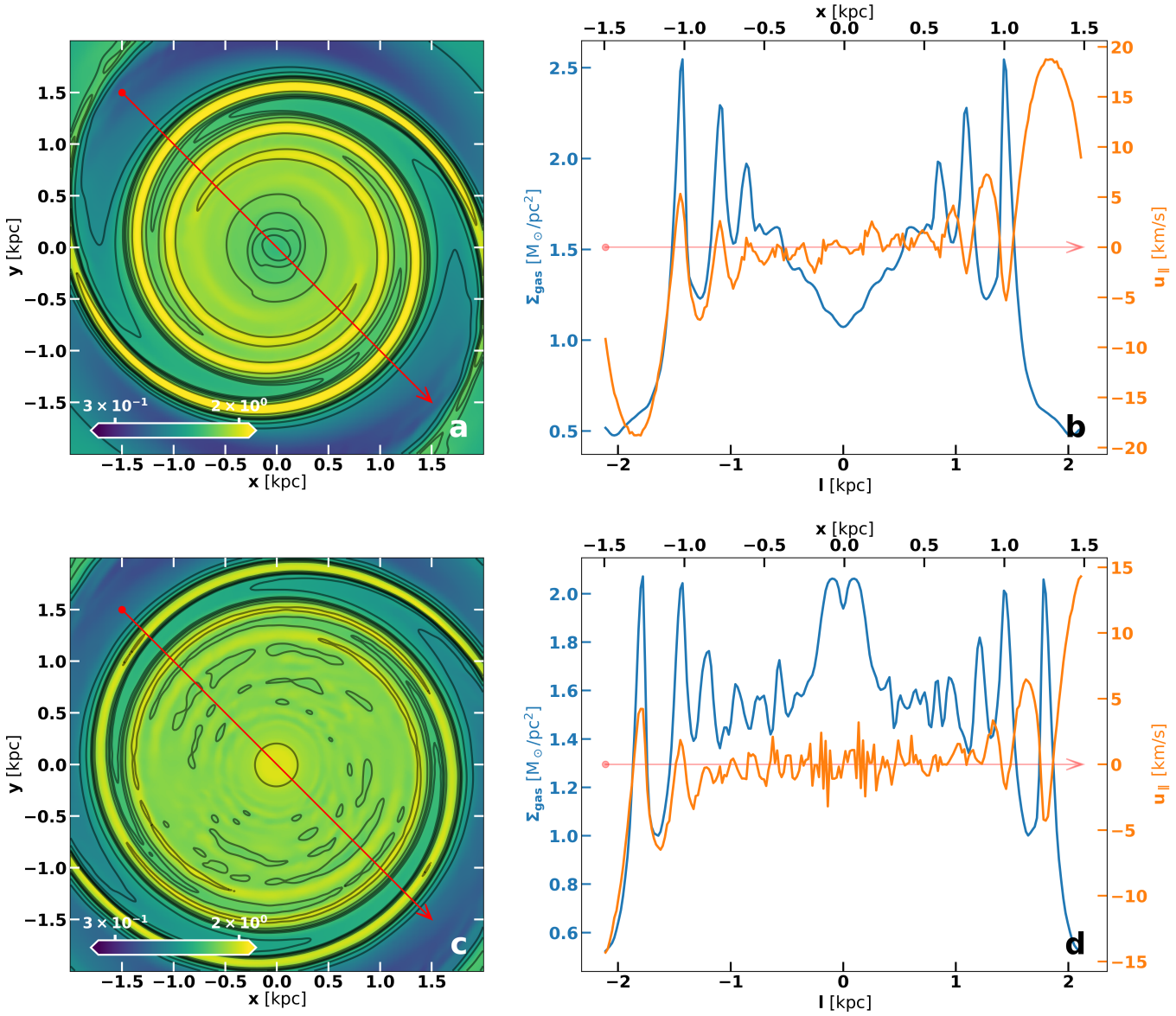

Fig. 23. (a) and (b): Variation in gas surface density (Σ) and the velocity component along a defined slit ($u_\parallel$) for model R801 with $c_s = 10\,\mathrm{km\,s^{-1}}$. (c) and (d) Same figures for model R991. We find that if a high surface density is initially set at the center (R991), it persists throughout the simulation; without it (R801), the central density remains low, lower than that of its surroundings, as in the case with the full potential.

spiral segments can naturally arise from the radius-dependent phase shift of damped closed gaseous orbits under specific resonance conditions.

In our simulations, leading spiral structures are evident in models with $c_s \lesssim 10\,\mathrm{km\,s^{-1}}$, particularly in those characterized by relatively strong barred perturbations. As the non-axisymmetric forcing weakens, the prominence of the leading spirals correspondingly diminishes. Such spirals may coexist with nuclear rings in the low-c_s models (e.g., in the fiducial case, Fig. 5), and they can also be identified in the innermost regions of models that otherwise develop trailing nuclear spirals (e.g., in the weak bar case, Fig. 13). By contrast, in models with $c_s = 20\,\mathrm{km\,s^{-1}}$, the leading spiral arms are no longer discernible. At this higher sound speed, the gas response favors the development of more open spiral structures, with reduced winding, and the loci of gaseous shocks are significantly displaced relative to the x_2 orbital domain (cf. Maciejewski 2004a). Under these conditions, the formation of leading spirals is suppressed (see also Kim et al. 2012b). Interestingly, in such models we consistently observe the emergence of a "twin peaks" morphology, suggesting that a possible link between the occurrence of leading spirals and twin peaks warrants further investigation.

7. In all models, while strong shocks are identified in the main body of the bar, the shocks in the central region are weak or negligible. Our models suggest that gas is funneled by the dust-lane shocks in the bar's main body into the ILR region. Over time, this process causes gas to accumulate either in the arcs of nuclear (pseudo-)rings or in the arms of tightly wound trailing spirals that diminish near the center. In models with high initial ρ_c, gas brought to the center compresses the existing central gas into smaller radii, further concentrating it near the center. This is a mechanism that promotes the concentration of gas near the center of the system.

This process offers an explanation for the formation of twin-peak features identified in some models. As shocks in the main body of the bar drive more gas into the ILR region, the compressed gas contributes to these features. This happens either along the arcs of (pseudo-)rings that extend as continuations of the dust-lane shocks, or close to the center in models with high central surface densities.

8. A key conclusion is that the parameters of a gravitational potential alone are insufficient to predict the gas dynamics of a model. The morphology of the gaseous response varies significantly with different sound speeds, highlighting the pivotal role of hydrodynamics in shaping the structure of the gas in the central region, in agreement with the results of Wada (1994), Kim et al. (2012b), Sormani et al. (2024).
9. The models used in this study primarily highlight tendencies in the development of response characteristics. Nevertheless, an overall evaluation suggests that features in the central regions of these models align best with observed galaxy morphologies for an assumed sound speed of $c_s = 20\,\mathrm{km\,s^{-1}}$. On the other hand, tightly wound spirals with an azimuthal extent significantly surpassing 2π, such as those present in several models, are rarely observed in galaxies. Their connection to the tightly wound nuclear spirals described by Martini et al. (2003a,b) requires further investigation.

Acknowledgements. We thank the anonymous referee for constructive comments on our manuscript. PAP would like to thank MPA for the opportunity to visit and work on parts of this project while at the institute. This work was funded by the Sectoral Development Program (ΟΠΣ 5223471) of the Greek Ministry of Education, Religious Affairs and Sports, through the National Development Program (NDP) 2021-25. It was conducted as part of project 200/1025, supported by the Research Committee of the Academy of Athens.

References

Ann, H. B., & Thakur, P. 2005, ApJ, 620, 197
Athanassoula, E. 1992a, MNRAS, 259, 328
Athanassoula, E. 1992b, MNRAS, 259, 345
Buta, R. 2013, in Planets, Stars and Stellar Systems, eds. T. Oswalt, & W. Keel (Springer Science+Business Media Dordrech), Extragalactic Astronomy and Cosmology, 6, 1
Buta, R., & Combes, F. 1996, Fund. Cosmic Phys., 17, 95
Combes, F. 2002, arXiv e-prints [arXiv:astro-ph/0208113]
Combes, F. 2022, Eur. Phys. J. Web Conf., 265, 00047
Comerón, S., Knapen, J. H., Beckman, J. E., et al. 2010, MNRAS, 402, 2462
Contopoulos, G. 1979, A&A, 71, 221
Contopoulos, G. 1980, A&A, 81, 198
Contopoulos, G. 1988, A&A, 201, 44
Contopoulos, G. 2002, Order and chaos in Dynamical Astronomy (Berlin: Springer)
Davies, R. I., Maciejewski, W., Hicks, E. K. S., et al. 2009, ApJ, 702, 114
Díaz, R. J., Dottori, H., Vera-Villamizar, N., & Carranza, G. 2003, ApJ, 597, 860
Englmaier, P., & Gerhard, O. 1997, MNRAS, 287, 57
Fathi, K., Storchi-Bergmann, T., Riffel, R. A., et al. 2006, ApJ, 641, L25
Ferrers, N. 1877, Q. J. Pure Appl. Math., 14, 1
Few, C. G., Dobbs, C., Pettitt, A., & Konstandin, L. 2016, MNRAS, 460, 4382
Fragkoudi, F., Athanassoula, E., & Bosma, A. 2016, MNRAS, 462, L41
Gingold, R. A., & Monaghan, J. J. 1977, MNRAS, 181, 375
Goldreich, P., & Tremaine, S. 1978, ApJ, 222, 850
Goldreich, P., & Tremaine, S. 1979, ApJ, 233, 857
Grosbøl, P. 2003, in Galaxies and Chaos, eds. G. Contopoulos, & N. Voglis, 626, 201
Hénon, M. 1965, Annales d'Astrophysique, 28, 992
Kenney, J. D. P., Wilson, C. D., Scoville, N. Z., Devereux, N. A., & Young, J. S. 1992, ApJ, 395, L79
Kim, W.-T., Seo, W.-Y., & Kim, Y. 2012a, ApJ, 758, 14
Kim, W.-T., Seo, W.-Y., Stone, J. M., Yoon, D., & Teuben, P. J. 2012b, ApJ, 747, 60
Knapen, J. H., Beckman, J. E., Shlosman, I., et al. 1995a, ApJ, 443, L73
Knapen, J. H., Beckman, J. E., Heller, C. H., et al. 1995b, ApJ, 454, 623
Kolcu, T., Maciejewski, W., Gadotti, D. A., et al. 2023, MNRAS, 524, 207
Kuzmin, G. 1956, Astron.Zh, 33, 27
Li, Z., Shen, J., & Kim, W.-T. 2015, ApJ, 806, 150
Lucy, L. B. 1977, AJ, 82, 1013
Maciejewski, W. 2004a, MNRAS, 354, 883
Maciejewski, W. 2004b, MNRAS, 354, 892
Maciejewski, W., Teuben, P. J., Sparke, L. S., & Stone, J. M. 2002, MNRAS, 329, 502
Martini, P., Regan, M. W., Mulchaey, J. S., & Pogge, R. W. 2003a, ApJS, 146, 353
Martini, P., Regan, M. W., Mulchaey, J. S., & Pogge, R. W. 2003b, ApJ, 589, 774
Pastras, S. 2022, Masters Thesis, University of Athens, Greece
Pastras, S., Patsis, P. A., & Athanassoula, E. 2022, Universe, 8, 290
Patsis, P. A., & Athanassoula, E. 2000, A&A, 358, 45
Patsis, P. A., & Hiotelis, N. 1994, in Ergodic Concepts in Stellar Dynamics, eds. V. G. Gurzadyan, & D. Pfenniger, 430, 261
Patsis, P. A., Contopoulos, G., & Grosbol, P. 1991, A&A, 243, 373
Patsis, P. A., Athanassoula, E., & Quillen, A. C. 1997, ApJ, 483, 731
Patsis, P. A., Xilouris, E. M., Alikakos, J., & Athanassoula, E. 2021, A&A, 647, A20
Piner, B. G., Stone, J. M., & Teuben, P. J. 1995, ApJ, 449, 508
Prieto, M. A., Maciejewski, W., & Reunanen, J. 2005, AJ, 130, 1472
Regan, M. W., & Teuben, P. 2003, ApJ, 582, 723
Slyz, A. D., Kranz, T., & Rix, H.-W. 2003, MNRAS, 346, 1162
Sormani, M. C., Binney, J., & Magorrian, J. 2015a, MNRAS, 449, 2421
Sormani, M. C., Binney, J., & Magorrian, J. 2015b, MNRAS, 451, 3437
Sormani, M. C., Binney, J., & Magorrian, J. 2015c, MNRAS, 454, 1818
Sormani, M. C., Sobacchi, E., & Sanders, J. L. 2024, MNRAS, 528, 5742
Stone, J. M., & Gardiner, T. 2009, New A, 14, 139
Stone, J. M., Gardiner, T. A., Teuben, P., Hawley, J. F., & Simon, J. B. 2008, ApJS, 178, 137
Teyssier, R. 2002, A&A, 385, 337
Toomre, A. 1963, ApJ, 138, 385
van Albada, G. D., van Leer, B., & Roberts, W. W. J. 1982, A&A, 108, 76
van der Laan, T. P. R., Armus, L., Beirao, P., et al. 2015, A&A, 575, A83
Wada, K. 1994, PASJ, 46, 165
Wada, K., & Habe, A. 1992, MNRAS, 258, 82
Wada, K., & Habe, A. 1995, MNRAS, 277, 433
Wada, K., & Koda, J. 2001, PASJ, 53, 1163